Biophysical Journal
Article

Biophysical Society

Effect of Post-Translational Modifications and Mutations on Amyloid-β Fibrils Dynamics at N Terminus

Liliya Vugmeyster,[1,*] Dan F. Au,[1] Dmitry Ostrovsky,[2] Brian Kierl,[1] Riqiang Fu,[3] Zhi-wen Hu,[4] and Wei Qiang[4]
[1]Department of Chemistry and [2]Department of Mathematics, University of Colorado Denver, Denver, Colorado; [3]National High Field Magnetic Laboratory, Tallahassee, Florida; and [4]Department of Chemistry, Binghamton University, Binghamton, New York

ABSTRACT We investigate the variability in the dynamics of the disordered N-terminal domain of amyloid-β fibrils (Aβ), comprising residues 1–16 of Aβ_{1-40}, due to post-translational modifications and mutations in the β-bend regions known to modulate aggregation properties. Using ^{2}H static solid-state NMR approaches, we compare the dynamics in the wild-type Aβ fibrils in the threefold symmetric polymorph with the fibrils from three post-translational modification sequences: isoaspartate-D7, the phosphorylation of S8, and an N-terminal truncation ΔE3. Additional comparisons are made with the mutants in the β-bend region (residues 21–23) corresponding to the familial Osaka E22Δ deletion and D23N Iowa mutation. We also include the aggregates induced by Zn^{2+} ions. The dynamics are probed at the F4 and G9 positions. The main motional model involves two free states undergoing diffusion and conformational exchanges with the bound state in which the diffusion is quenched because of transient interactions involving fibril core and other intrastrand contacts. The fraction of the bound state increases in a sigmoidal fashion with a decrease in temperature. There is clear variability in the dynamics: the phosphorylation of S8 variant is the most rigid at the G9 site in line with structural studies, the ΔE3 fibrils are more flexible at the G9 site in line with the morphological fragmentation pattern, the Zn-induced aggregates are the most mobile, and the two β-bend mutants have the strongest changes at the F4 site toward higher rigidity. Overall, the changes underlie the potential role of conformational ensembles in setting the stage for aggregation-prone states.

SIGNIFICANCE In this work, we demonstrate variations of motions in the disordered region of amyloid-β fibrils due to modifications induced either by naturally occurring mutations or post-translational modifications. The results indicate a clear variability in the flexibility of the disordered domain and its potential role in modulating aggregation-prone states.

INTRODUCTION

Amyloid-β peptide (Aβ) aggregation remains to be viewed as one of the causative factors in Alzheimer's disease (AD) as a part of the amyloid hypothesis (1–4). It is believed that Aβ accumulation is a trigger that initiates a pathological cascade implicating τ protein, synuclein, and other aggregation-prone proteins (2,3). The structural polymorphism of amyloid fibrils is a challenging and potentially pathologically important factor in the molecular basis of AD (5–9). This polymorphism occurs at multiple levels (10), leading to many possible fibrillar structures from the same Aβ protein as well as the existence of multiple molecular variants of Aβ, including 1–39, 1–40, and 1–42, and the variants of these with post-translational modifications (PTMs) and mutations. The majority of PTMs occur in the flexible N-terminal region of the fibrils, encompassing residues 1–16, and are thought to trigger or accelerate the fibrillation of wild-type Aβ peptides (2,11,12). However, the pathological roles of modified Aβ in AD have not been determined in detail. It has been suggested that PTMs may be responsible for sporadic cases of AD, which encompass 90% of all patients (2,11). On the contrary, many familial-type mutations that cause the early onset of the disease occur around the β-bend region of Aβ, comprising residues 21–23, and are associated with altered folds, higher aggregation propensities, and higher toxicities (13–16). Metal ions are also known to alter aggregation propensities. In particular, animal models show that Zn^{2+} coordination can play a crucial role in the formation of plaques in vivo (17–19). At the

Submitted July 18, 2019, and accepted for publication September 9, 2019.
*Correspondence: liliya.vugmeyster@ucdenver.edu
Editor: Keir Neuman.
https://doi.org/10.1016/j.bpj.2019.09.004

concentrations of what is found at the synapses, Zn^{2+} specifically binds to Aβ and promotes aggregation (20,21). The resulting multitude of the structural ensembles, combined with the differential seeding abilities of the variants, can have profound implications on the existence of the most aggressive forms as well as on the effectiveness of the initiation of the pathological cascades of the aggregation of other related proteins.

One of the ways in which to characterize the ensembles is probing the flexibility of the structures (10). We compare the dynamics in wild-type Aβ_{1-40} in one of its more toxic polymorphs possessing threefold symmetry (22) with two PTMs occurring around the "hot-spot" six to eight region (10) of the N-terminal domain, an N-terminal truncation PTM, and two mutants corresponding to familial mutations in the β-bend 21–23 region of the fibrils. In particular, we investigate PTMs corresponding to the phosphorylation of S8 (pS8) and aspartate to isoaspartate at position D7 (isoD7); the truncation variant corresponds to the cleavage of the peptide bond between positions 2 and 3 (ΔE3) as well as the Osaka E22Δ deletion mutant and D23N Iowa mutant of the β-bend region. Additionally, we include in the comparison the results for the aggregates formed by wild-type Aβ_{1-40} in the presence of Zn^{2+} ions (Zn). Below, we present the relevant backgrounds of these variants.

The E22Δ Aβ_{1-40} deletion mutation has been found to be more neurotoxic in rat primary neuron cultures than wild-type Aβ (23). Previous works have characterized the twofold symmetric structure displaying the in-register parallel β-sheet as well as determined the mass per length (MPL) measurements (24). The cross section of the fibril can be approximated by a rectangle defined by an additional intermolecular salt bridge between the Glu3 and Lys28 side chains, which seems to be absent in wild-type models. A unique feature of the fibrils is that they form extremely fast and show very low levels of thioflavin T fluorescence with no lag phase (25). The E22Δ variant has also been shown to efficiently cross-seed the wild-type protein (26).

One of the essential features of the D23N Aβ_{1-40} Iowa mutant is its ability to form an antiparallel β-sheet structure (27–30). The polymorph of D23N with the antiparallel β-sheet structures are relatively short and curved fibril-like intermediates. They are metastable and eventually convert into mature D23N fibrils, which have parallel β-sheet structures similar to wild-type Aβ fibrils (28,30,31). The structural unit is a monomer in this case. The hydrophobic core is somewhat less compact than the wild-type.

The pS8 modification has recently been shown to have a strong cross-seeding ability for wild-type Aβ (32), and its structure as well as the dynamics of the core region have been determined by solid-state NMR (33). S8 phosphorylation has been shown to play an important role in late-onset sporadic AD (34,35) and is especially associated with the symptomatic pathology (36). It may also display increased nucleation-dependent fibrillation and enhance Aβ-mediated toxicity (11,37). The pS8 fibrils show the twofold symmetric structure with the in-register parallel β-sheet and striated-ribbon morphology similar to the twofold wild-type Aβ_{1-40} when grown under similar conditions (33). However, the fibrils are ~2.5 nm wider. The highest structural distinction were observed in the N-terminal region. In particular, the variant showed strong intrastrand interactions between the N-terminus and the rest of the amyloid core. Additionally, the hydrophobic core packing was more pronounced than the wild-type, and the side-chain dynamics were more restricted in the core.

The isoD7 PTM has been found to increase aggregation propensities and zinc-dependent oligomerization (12,38,39). In parenchymal plaque core preparations, isoaspartate is the predominant form at position number 7 (12,40). In vitro, this type of isomerization has also been suggested to lead to an enhanced propensity to form β-sheets as well as an enhanced insolubility and resistance to enzymatic degradation (12,41–43). The intriguing study by Fonseca et al. suggested that the amount of isoD7 in plaques can serve as an indication of plaque age (44). Fukuda et al. (42) demonstrated that Aβ_{1-42} does not form fibrils in the presence of isoD7 modification. In this study, we work with the isoD7 sequence cross-seeded with wild-type Aβ_{1-40} to promote fibrillation. For this variant, as the structure is not available, we supplement an NMR investigation with the MPL characterization of these fibrils based on tilted beam transmission electron microscopy (TEM) measurements (45).

It has been suggested that the shortening of the N-terminus may lead to a higher aggregation propensity (12,46,47). One example is the 3-glutamate truncation (ΔE3) seen in plaques originating from late AD cases as well as in mouse-based models of AD (48). This truncation also serves as a starting point for the generation of the pyroglutamate-3 aggressive modification. The enhanced aggregation propensity in these PTMs may be at least partially attributed to the reduced polarity and enhanced hydrophobicity from the deletion of charged residues at N-termini (47). Morphologies and fibrillation kinetics have been found to be similar between the ΔE3 and pyroglutamate-3 variants and in general faster than the fibrillation of other N-terminal PTM subtypes (49). Scheidt et al. (50) utilized solid-state NMR to compare the structures of the pyroglutamate-3 and the wild-type fibrils and concluded that the cores are rather similar structurally, although the N-terminus shows an alteration in the dynamics based on the backbone order parameters probed at the C_α sites. This study did not tackle the ΔE3 precursor itself, however.

This work focuses on investigating the dynamics of the flexible N-terminal region of the fibrils, which is known to be important for the regulation of aggregation control (51–57). The general flexibility of noncore regions in Aβ has been demonstrated by multiple techniques, such as NMR (58–66), electron paramagnetic resonance (67), hydrogen-deuterium exchange (68–70), x-ray crystallography (71),

and fluorescence spectroscopy (72). Fawzi et al. utilized solution NMR saturation transfer approaches to probe the binding of monomeric Aβ to the surface of protofibrils (73,74). The site-specific characterization of dynamics in aggregated forms remains challenging because of the difficulties of obtaining site-specific resolution. Many structures (including wild-type structures) (60) have been unable to include the first nine residues of Aβ because of the mobility of these sites.

We recently investigated the dynamics of the N-terminal subdomain in wild-type fibrils by probing the motions of hydrophobic side chains using ^{2}H solid-state NMR methods combined with residue-specific deuteration (75,76). The N-terminal domain participates in a number of motional modes, including the overall diffusion-like motion at two different timescales and the conformational exchange process that could be attributed to the transient interactions of the N-terminal domain with the structured hydrophobic core. At 37°C, we observed a progressive freezing of the dynamics along the sequence, characterized by an increased fraction of the bound state and reduction in the overall diffusive motion of the domain.

The goal of this work is the detailed comparison of the N-terminal domain dynamics among the variants described above. The dynamics are probed at the F4 site belonging to the more flexible N-terminal end and the G9 site at which the dynamics are significantly reduced in wild-type fibrils (Fig. 1; (76)). The differential dynamics in all these variants underscores conformational sampling, which likely contributes to differentiating the aggregation propensities and cross-seeding aggressiveness.

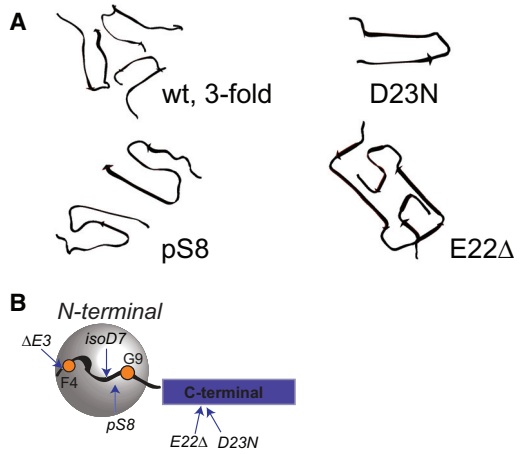

FIGURE 1 (*A*) Quaternary structure for the variants studied in this work for which the structural coordinates are available: wild-type threefold symmetric structure (Protein Data Bank [PDB]: 2LMP) (22); pS8 PTM with the twofold symmetric structure (PDB: 6OC9) (33); monomeric structure of the Iowa D23N mutant with the antiparallel β-sheet structure (PDB: 2LNQ) (30); and Osaka E22Δ mutation with the rectangular cross section (PDB: 2MVX) (24). (*B*) Shown is a schematic representation of the domains of Aβ_{1-40}, with the flexible N-terminal domain (residues 1–16, *gray sphere*) and C-terminal domain spanning the core (*blue rectangle*). Modified sequences investigated in this work are marked with arrows; ΔE3, isoD7, and pS8 are located in the N-terminal domain, and E22Δ and D23N are located in the β-bend region of the C-terminal domain. The sites of the deuterium isotope labels on the side chains of F4 and G9 are shown as orange dots. The labeling patterns are ring-D_5 for F4 and $^{\alpha}CD_2$ for G9. To see this figure in color, go online.

MATERIALS AND METHODS

Peptide synthesis

The Aβ_{1-40} peptides were prepared by using solid-state peptide synthesis (performed by Thermo Fisher Scientific, Rockford, IL). Fluorenylmethyloxycarbonyl-phenylalanine-ring-d_5 and fluorenylmethyloxycarbonyl-glycine-C_α-d_2 were purchased from Cambridge Isotopes Laboratories (Andover, MA). Further details are listed in the Supporting Materials and Methods. The resulting peptides had isotopic labels in only one chosen residue, either F4 or G9.

Fibrils preparation

The pS8 and ΔE3 fibrils were grown following the generation seeding protocol developed previously (33,77). IsoD7 cross-seeded with wild-type Aβ_{1-40}; the seeds consisted of the wild-type Aβ_{1-40} fibrils in the threefold symmetric polymorph and were used in 1:10 molar ratio of the wild-type Aβ_{1-40} seeds to the isoD7. E22Δ fibrils were prepared at 0.3 mg/mL concentration, and TEM images were taken immediately upon dissolving in the buffer and at 2–3 h and 24–30 h after dissolution. Details of these procedures are listed in the Supporting Materials and Methods. Preparation of the D23N fibrils with antiparallel β-sheet structure utilized a two-step seeding/filtration cycle that takes advantage of the differences in fibril formation rate between the parallel and antiparallel structures (30). Zn^{2+}-induced aggregates were prepared as described in the earlier work (76). After pelleting and lyophilizing of the fibrils, the hydrated state with a water content of 200% by weight was achieved by pipetting deuterium-depleted H_2O. The samples were packed in 5-mm NMR tubes (cut to 21-mm length) using Teflon tape to center the sample volume in the coil of the NMR probe.

NMR spectroscopy

Line shape experiments were performed with a quadrupole echo pulse sequence (78). The $R_{1\rho}$ experiments were performed at 9.4 T and 37°C using the methodology described in previous work (79) with the pulse sequence of Fig. S1. The relaxation decay curves $M(t)$ corresponding to the integration of the central narrow component (up to the half-height intensity) were fitted to a single exponential function with an offset: $M(t) = Ae^{-t/T_{1\rho}} + B$. ^{2}H QCPMG time domain measurements (Fig. S1) (80) were performed at 14.1 T field strength and 37°C. Integrated echo intensities were fitted to a single exponential function with no offset. Further details are listed in Supporting Materials and Methods.

Fitting of freezing curves

The data for p_{bound} were fitted to the function as follows:

$$p_{bound} = a + \frac{b-a}{1+\exp\left(\frac{T-T_m}{\sigma}\right)}, \quad (1)$$

in which T_m is the midpoint of the freezing curve, σ is the characteristic width of the transition region, and a and b are the higher and lower temperature baselines, respectively.

RESULTS

Morphological patterns

The fibrils of the Aβ_{1-40} variants (Fig. 1) exhibited different morphological patterns characterized by the negatively stained TEM technique (Fig. 2, additional images in Fig. S2), consistent with the findings in the literature and our previous work (25,30,32,33,81–83). The twisted threefold symmetric morphology of the wild-type fibrils (Fig. 2, previous analysis of the wild-type fibrils (76,83)) contrasts with the straighter and thicker fibril filaments for the pS8 fibrils, relatively short straight fibrils for the ΔE3, curvy and short D23N fibrils, long and curvy E22Δ fibrils, and amorphous Zn^{2+}-induced aggregates. Two additional observations are worth noting; for the E22Δ mutant, the fibrils reached the final morphologies in 2–3 h (Fig. S3), in line with previous studies (25). In addition, the fragmentation pattern observed for the ΔE3 morphology was similar to that of the pyroglutamate-3 fibrils (Fig. S4; Wulff et al. (49)).

For the isoD7 variant cross-seeded with wild-type threefold Aβ, the morphology was largely conserved. To further quantify the dimensions of the fibrils resulting from cross-seeding isoD7 with the wild-type fibrils in the threefold polymorph, we performed a detailed MPL analysis. Specifically, we employed tilted beam TEM (dark-field imaging), which is effective for the statistical characterization of the MPL of fibrils (45,84,85). Both the twofold and the threefold polymorphs of native Aβ_{1-40} (60,81) have previously been analyzed using this technique (45). The results (Fig. S5) indicated that the predominant polymorph is closer in its MPL to the threefold wild-type variant (around 90% of the fibrils), with a small proportion of the twofold characteristics. Further studies are needed to assess whether this trend is general; in this study, we suffice with characterization of our bulk samples used in the NMR analysis.

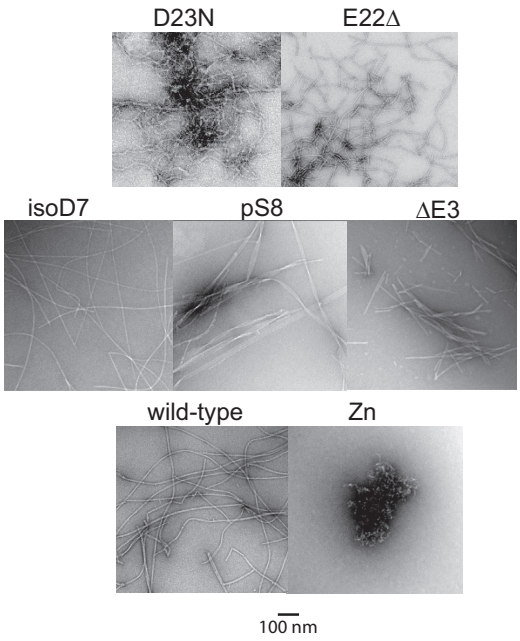

FIGURE 2 Typical examples of the negatively stained TEM images of fibrils from different variants investigated in this study.

Overview of the general model of N-terminal flexibility and approaches

For each of the fibril types, two samples were prepared for the NMR analysis: one containing a deuterium label at the F4 position, ring-D_5, and another at the G9 position, $^{\alpha}CD_2$.

We recently demonstrated that ^2H rotating frame relaxation ($R_{1\rho}$) and quadrupolar Carr-Purcell-Meiboom-Gill (QCPMG) transverse relaxation measurements provide a comprehensive view of conformational exchange processes (75). Although both these techniques are sensitive to motions on the biologically relevant μs-ms timescales, they provide complementary information on the motional modes.

In this section, we review the motional models employed to fit all the experimental data. The motional model in Fig. 3 *A*, which was developed based on the data for the wild-type protein (75), includes three states of the N-terminal domain: two "free" mobile states in which the N-terminal undergoes large-angle diffusion motion and one bound state in which the diffusive motion in quenched, most likely because of transient interactions with the structured fibril core or transient intrastrand interactions with N-terminal domains of neighboring chains (Fig. 3 *D*). In the free state, restricted rotational diffusion is very pronounced, and we assume an isotropic scenario for the local motional axis (i.e., phenyl axis for the case of F4 and twofold rotation axis for the case of G9 CD_2 group). This is not to be confused with global isotropic diffusion of macromolecules in solution—the fibrils are only 200% by weight hydrated with most of the water contributing to the hydration shell.

The diffusion coefficients in the two free states differ by about two orders of magnitude difference between the two states, $D_1 \gg D_2$. Each of the free states undergoes a conformational exchange process with the bound state, with the rate constants of $k_{ex,1}$ and $k_{ex,2}$, respectively. For the G9 sites, in two of the variants, this model cannot fit the data. For the Zn-induced aggregates, no conformational exchange that involves the bound state is detected; rather, the exchange between the two free states is invoked (Fig. 3 *B*). For the D23N fibrils, only a single free state has the "slow" diffusion coefficient of D_2 (Fig. 3 *C*).

The model of Fig. 3 *A* has been developed as the simplest scheme based on the extensive data on the dynamics of the wild-type Aβ fibrils. It does not incorporate any structural constraints other than a physical intuition on what would be, in general, consistent with the known structures of the fibrils. In particular, we do not assume any specific structural constraints for the transient interactions between the free and bound states. Additionally, the approximation of the isotropic diffusion and two different conformational

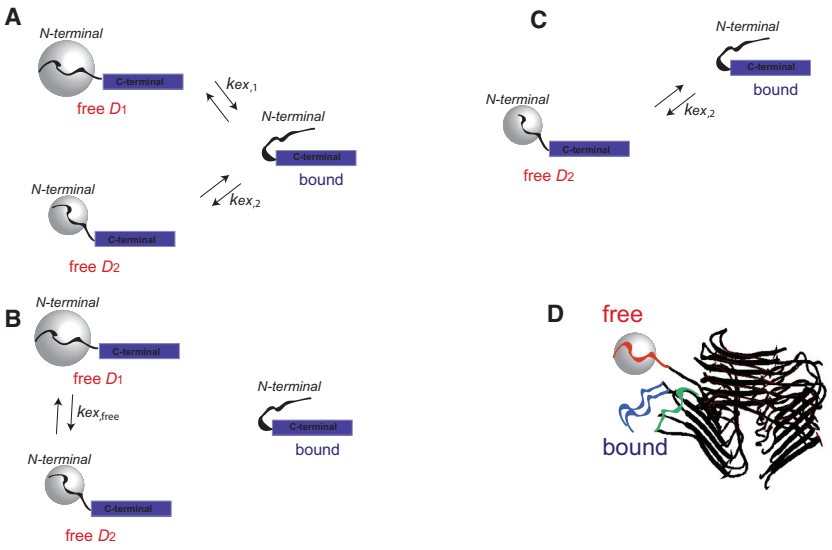

FIGURE 3 Modeling schemes for the motions of the disordered N-terminal domain (residues 1–16) of the Aβ_{1-40} fibrils. (*A*) Three-state motional model in which the N-terminal domain (*curved line*) transiently interacts with the structured C-terminal domain (*blue rectangle*) (75). In the two free states, the N-terminal domain is assumed to undergo isotropic diffusion with the diffusion coefficients D_1 and D_2, $D_1 \gg D_2$, represented by the gray spheres, whereas in the bound state, the interactions quench this mode. The timescales of the interactions are given by the two chemical exchange rate constants $k_{ex,1}$ and $k_{ex,2}$, respectively. Most sites were fit with this full model. (*B*) Shown is a modification of model A for which there is no conformational exchange between the free and bound states on the experimental timescales but instead exchange between the two free states with the rate constant $k_{ex,free}$, which is applicable to the Zn^{2+} aggregates at the G9 site. (*C*) Shown is the submodel of (*A*) in which there is no fast free diffusion state, only a slow free diffusion state, which is applicable to the D23N sample at the G9 site. (*D*) Shown is a schematic representation of free (*orange wiggly line*) and bound (*blue and green wiggly lines*) states of N-terminal subdomain with the threefold wild-type fibrils structure. The threefold symmetric fibril core is taken from PDB: 2LMP (22) and is shown as a black ribbon diagram. The bound state can arise either because of transient interactions with the core (*green lines*) or transient tight stacking with the neighboring N-terminal strand (*blue lines*). In the free state (*orange wiggly line*), the domain can undergo relatively large-scale fluctuations, which are not possible in any of the bound states. To see this figure in color, go online.

states of the N-terminal domain is possibly reflecting a much more complex situation with anisotropic motions and an ensemble of multiple states, in analogy to the existence of tethered states found for monomers on the surface of protofibrils (73,74). Within the available dynamics data, invoking these more complex models would be a clear overfitting of the data. For consistency, we keep the model the same for all of the Aβ variants, unless a clear need arises to introduce modifications based on the data. We also note that the line shape data alone could be modeled based on an assumption of two static nonexchanging fractions with rigid and motionally narrowed tensors. However, our previous analysis of the longitudinal relaxation data for the wild-type fibrils in conjunction with $R_{1\rho}$ measurements precludes the use of such a model.

We show that depending on the quadrupolar interaction magnitude and timescale of motion, QCPMG and $R_{1\rho}$ experiments are sensitive to different conformational exchange processes. For the F4 residues, the effective quadrupolar tensor is narrow, with an effective quadrupolar coupling constant of $C_q = 36.6$ kHz after averaging over the rotameric motions of the side chain. On the contrary, for the G9, the effective C_q is 77.6 kHz after averaging over the two-site jumps of the CD_2 group. As a result, the QCPMG experiment primarily probes the conformational exchange between the free state with a fast diffusion state and the bound state (D_1, rate constant $k_{ex,1}$) for the F4 sites and the free slow diffusion state and the bound state (D_2, rate constant $k_{ex,2}$) for the G9 sites. The situation is reversed for the $R_{1\rho}$ experiment; it is most sensitive to the conformational exchanges between the fast diffusion free state and bound state for the G9 sites as well as between the slow diffusion state and bound state for the F4 sites. The relative populations of the two free states are obtained by fitting the data to the full model in Fig. 3 *A*.

The fraction of the bound state p_{bound} was taken from the line shape analysis. p_{bound} as a function of temperature follows a sigmoidal curve indicative of a relatively abrupt freezing of the diffusion motions. This approach is not based on any assumptions regarding possible structural changes induced by lowering the temperature (i.e., p_{bound} only reports on the cumulative increase of intra- and intermolecular interactions that lead to line broadening). The midpoint freezing temperature T_m (see Eq. 1) increases along the N-terminal domain chain for the wild-type protein. Although, for the residues close to the N-terminal end (A2 to H6 sites), it appears to be dictated by the freezing of the hydration layer (~267 K), T_m increases along the sequence and is at 284 K for the G9 (76). p_{bound} at the physiological temperature increases from 8 to 10% in the A2–H6 region, to 35% for the G9, and to 85% at the V12 site. Thus, to probe the dynamics of all the variants, we selected labels at the F4 and G9 locations to capture the details of the dynamics in the more flexible N-terminal domain region and the region in which the dynamics can be more restricted because of more pronounced interactions with the core. $R_{1\rho}$ measurements are conducted for four values of spin-locking field strength and QCPMG measurements for at least seven values of interpulse spacing. Between these relaxation data and p_{bound} determination from the line shape analysis, there are enough data points to determine all model parameters.

^{2}H NMR line shape analysis yields the fraction of the bound state

The ^{2}H line shape is a simple one-dimensional experiment performed with a quadrupolar echo pulse sequence (78) that provides a wealth of information on the dynamics close to the timescale of the effective quadrupolar coupling constant. At the physiological temperature, for all variants, the line shapes significantly narrow and they approach solution-like line shapes (Fig. 4), indicating the presence of large-scale motions on the relevant timescale. With a decrease in temperature, the wide component of the powder pattern becomes apparent. The narrow component is attributed to the free states undergoing motions approximated by the isotropic diffusion. The wide component is attributed to the "bound" state, which lacks diffusive motions, presumably because of interactions with the rigid fibril core. The p_{bound} for the F4 residue is quantified by decomposing the line shape into its Lorenzian and non-Lorenzian components (76), the latter of which is attributed to that of the bound state (see the examples in Fig. S6). Similar to the treatment of the wild-type fibrils (76), the analysis for the G9 sites is somewhat more complex, with p_{bound} spanning the subset of the non-Lorenzian contribution corresponding to the rigid pattern. Interestingly, for the pS8 G9 site at high temperatures, it appears that the bound state has a different chemical shift than the free states (Fig. S6). The p_{bound} for all residues (Fig. 5) follows the characteristic sigmoidal behavior observed for the wild-type protein, and this can be fitted to Eq. 1, which yields the midpoint of the freezing curves T_m and width of the transition σ, summarized in Fig. 6 along with the results for the fraction of the bound state p_{bound} at the physiological temperature.

The higher value of T_m signifies that the onset of the freezing of the diffusion motions starts at a higher temperature upon sample cooling. Most variants display a gap in T_m value between the F4 and G9 sites of 5–20°. For the ΔE3 fibrils, the value of T_m is 262–263 K for both sites; for D23N, it is 273 K for both sites (Fig. 6). The largest gap of 20° is for the pS8 fibrils. Interestingly, the width of the transition is maintained at a higher value for the G9 sites (average value of 7°) in comparison with F4 for all samples (with an average value of 2.1°). The higher values of σ may reflect stronger interactions with the core with a distribution of distances between the probed site and contacts within the core, leading to a wider transition. Further, the value of p_{bound} at 37°C is consistently higher (0.14–0.42) than that of F4 (0.06–0.18) for all samples (Fig. 6). There is a clear variability in the fitted values of T_m between the different Aβ variants. For example, the pS8 variant has the highest T_m and highest p_{bound} for the G9 site. This result is in line with a recent structural study (33) pointing to a more structured N-terminal domain. The T_m values at the G9 sites are much lower for the ΔE3, isoD7, and D23N variants. It is also of note that the line shapes at the physiological temperature are wider for the D23N variant for both sites, pointing to the possibility of a slower conformational exchange between the free and bound states, as detailed later in the text.

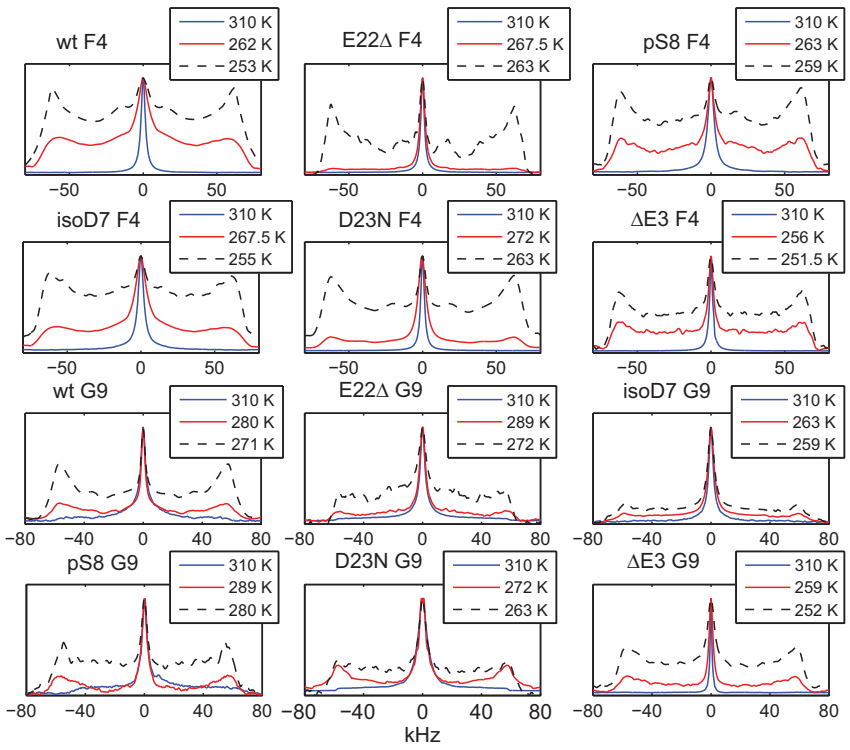

FIGURE 4 Representative ^{2}H static solid-state NMR line shape data in the hydrated fibril samples of Aβ_{1-40} at 310 K and two intermediate temperatures. The isotope labeling patterns are F4-ring-D_5 and G9-$C_\alpha D_2$. The data for the wild-type fibrils are taken from an earlier work (76). To see this figure in color, go online.

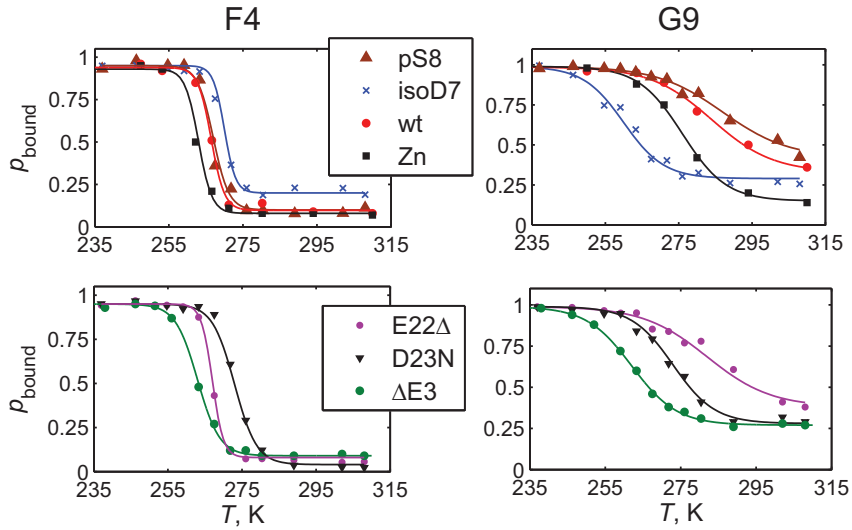

FIGURE 5 p_{bound} derived from the line shape decomposition as a function of temperature. The solid lines represent the fits according to Eq. 1. The data for the wild-type fibrils and Zn^{2+}-induced aggregates are taken from an earlier work (76). To see this figure in color, go online.

^{2}H QCPMG and $R_{1\rho}$ relaxation measurements provide the conformational exchange rate constants and diffusion coefficients of the free states

To probe the timescales of the conformational exchange and obtain the most accurate values of the diffusion coefficients, it is necessary to perform more complicated measurements known to be sensitive to conformational exchange processes at the μs to ms timescale, such as the QCPMG and $R_{1\rho}$ measurements (86–89) briefly described in Overview of the general model of N-terminal flexibility and approaches above. Our earlier work describes the technical details of these measurements and the fitting procedure based on the models using the full Liouvillian treatment of relaxation (75,79). Here, we focus on the results, which were obtained at the physiological temperature.

The ^{2}H QCPMG experiment under static conditions (see Supporting Materials and Methods; Fig. S1 *A*) is performed by measuring the transverse relaxation rates as a function of the spacing of the refocusing pulses, τ_{QCPMG}, using a time domain approach. Motions on the timescale of τ_{QCPMG} interfere with the refocusing of magnetization, and the extent of this interference depends on the interpulse spacing. Interestingly, the dispersion profiles are the reverse of those traditionally seen in solution CPMG experiments, likely because of the anisotropic nature of the quadrupolar interactions (75,88). For the ^{2}H $R_{1\rho}$

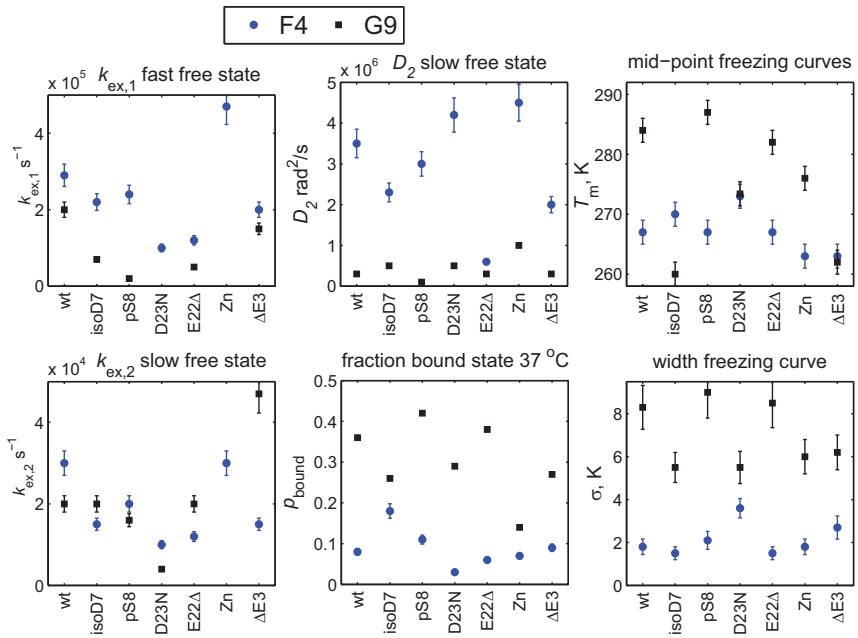

FIGURE 6 Summary of the model parameters according to the full model in Fig. 3 *A* and the fits of the freezing curves. The rate constants are $k_{ex,1}$, $k_{ex,2}$, D_2, p_{bound}, T_m, and σ. D_1 is in the fast limit and is at least 0.7–1 $\times$ 10^8 rad^2/s. The relative percentages of the populations of the free to slow diffusion state are as follows: 70/30 for the F4 sites of wild-type and Zn; 60/40 for the F4 sites of ΔE3, isoD7, E22Δ, and pS8; 20/80 for the F4 site of D23N; and 5/95 to 10/90 for all the G9 sites, except for D23N for which it is zero (see the model in Fig. 3 *C*) and Zn for which it is around 50/50. The Zn G9 site is fitted with the model in Fig. 3 *B* with $k_{ex,free} = 250$ s^{-1}. The errors were obtained by the inverse covariance matrix method calculated with Monte-Carlo sampling of the model parameters. Error bars smaller than the sizes of the symbols are not shown. To see this figure in color, go online.

experiment under static conditions (Fig. S1 *B*) (79), refocusing is accomplished by the variable spin-locking field, ω_{SL}.

Fig. 7 summarizes the experimental relaxation times, and Fig. S7 provides examples of the raw data. The variability between the samples is immediately apparent for both experiments. For the D23N sample at the G9 site, the $R_{1\rho}$ rate was too fast to be measured accurately.

As noted, defining the magnitude of the quadrupolar interaction is important because this governs which timescales can be obtained from the two experiments. For the G9 site, we used the tensor with a quadrupolar coupling constant C_q of 77.6 kHz and the asymmetry parameter $\eta = 1$, as previously determined (76). The tensor corresponds to the effective value averaged over fast two-site jumps of the CD_2 group, which followed from the longitudinal relaxation results for the wild-type samples. For F4, we started with the tensor corresponding to the averaging over the fast two-site π-flips of the ring, consistent with the longitudinal relaxation data. However, this tensor leads to rate constants for the F4 site in the wild-type fibrils that are orders of magnitude smaller than those found for the A2 and H6 sites, inferring the presence of additional motions that affect the QCPMG and $R_{1\rho}$ rates and lead to a lower effective C_q value. We thus invoke a two-site rotameric exchange involving the χ_1 and χ_2 dihedral angles. Specifically, we assume the existence of the rotamers found by Drobny and coworkers for one of the phenylalanine residues of the mineral recognition domain of the biomineralization protein salivary statherin adsorbed onto its native hydroxyapatite (90); conformer one has $\chi_1 = 186.2°$ and $\chi_2 = 88.6°$, whereas conformer two has $\chi_1 = 274.7°$ and $\chi_2 = 54.8°$. The ratio of the populations is taken as 1:1. In the fast limit, this leads to an effective tensor of $C_q = 36.6$ kHz and η of 0.94. This tensor provides diffusion coefficients and rate constants for the wild-type fibrils perfectly in line with those of the A2 and H6 residues, allowing us to conclude that the additional rotameric motion is a good approximation of the additional mode affecting the relaxation rates.

All the F4 sites followed the model in Fig. 3 *A*. For the G9 sites, there are two exceptions; as noted, D23N in the G9 site had a very fast $R_{1\rho}$ decay that could not be measured. Based on the analysis of the model for the wild-type fibrils (75), this signifies the almost complete absence of the fast diffusion state, and thus, this site is fitted with a single free state (Fig. 3 *C*). For the G9 site in the Zn^{2+}-induced aggregates, the model in Fig. 3 *A* cannot be used; however, the model in which the exchange is dominated by the two free states (Fig. 3 *B*) is adequate. The QCPMG-T_2 data are qualitatively different in this variant, with higher T_2 values and, most importantly, negligible dispersion.

The variations in the experimental rates are reflected in the fitted values of D_2, $k_{ex,1}$, and $k_{ex,2}$. Fig. 6 summarizes the main parameters of the model, and Fig. S8 provide examples of the fits of the experimental relaxation rates. The diffusion constant for the fast diffusion state D_1 is in the fast limit, and thus, we can only state its lower limit, which falls to 0.7–1 $\times$ 10^8 rad^2/s. The conformational exchange rate constant $k_{ex,1}$ for the wild-type for this state is 3×10^5 s^{-1} for the A2, F4, and H6 sites and 2×10^5 s^{-1} for the G9 sites. The variants' range for $k_{ex,1}$ is 1.2–4.7 $\times$ 10^5 s^{-1} for F4 and 0.7–5 $\times$ 10^5 s^{-1} for G9. The slow diffusion state values of D_2 are 3.5×10^6 rad^2/s and $3.0 \cdot \times 10^5$ rad^2/s for the wild-type F4 and G9 sites, respectively. The range of the variants is 0.6–4.5 $\times$ 10^6 rad^2/s for the F4 sites and 3–10 $\times$ 10^5 rad^2/s for the G9 sites. The conformational exchange rate constant $k_{ex,2}$ is 3×10^4 s^{-1} for the A2, F4, and H6 sites in the wild-type protein and 2×10^4 s^{-1} for G9. The ranges of the variants are 1–3 $\times$ 10^4 s^{-1} and 0.4–4.7 $\times$ 10^4 s^{-1} for the F4 and G9 sites,

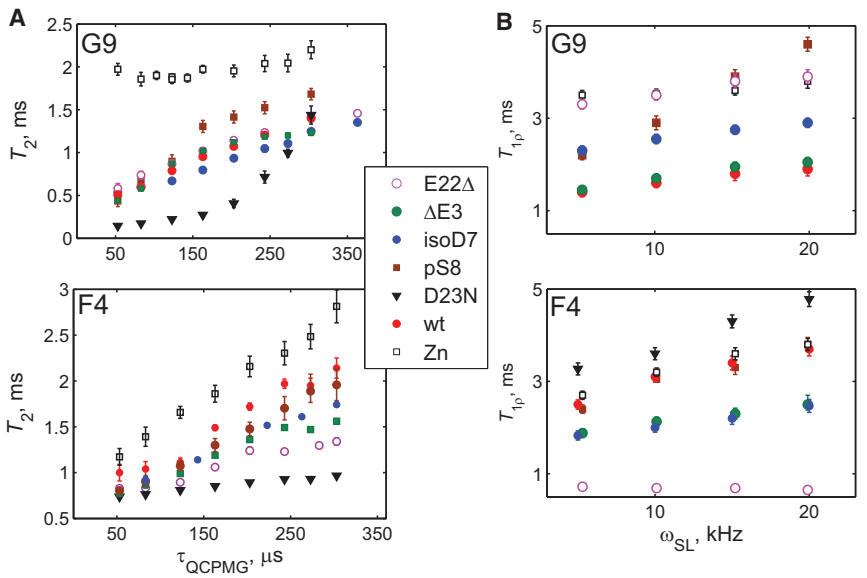

FIGURE 7 (*A*) Experimental transverse relaxation time T_2 as a function of τ_{QCPMG} in the hydrated fibril samples of $A\beta_{1-40}$ derived from the time domain QCPMG experiment, collected at 37°C and 14.1 T. (*B*) Experimental ^2H $T_{1\rho} = 1/R_{1\rho}$ relaxation times at 37°C and 9.4 T are shown. The errors in the rates were obtained by the inverse covariance matrix method. Error bars smaller than the sizes of the symbols are not shown. To see this figure in color, go online.

respectively. For the G9 site of the Zn^{2+}-induced aggregates, the exchange rate constant between the two free states (see model in Fig. 3 *B*) is 250 s^{-1}. The relative percentage of the fast to slow diffusion free states at the F4 site is the largest for the wild-type and Zn variants (70/30%) and decreases somewhat (60/40%) for the other variants, except for D23N in which it is drastically reduced to 20/80%. The fast state "freezes" to 5–10% for all samples for the G9 site and to zero for the D23N site, whereas it remains at around 50/50% for the Zn G9 site.

DISCUSSION

The N-terminal domain remains flexible for all the considered variants, and the models of motions are generally similar; however, the extent of this flexibility varies among sequences. The three-state model involving two free states undergoing isotropic diffusion and one bound state (Fig. 3 *A*) is applicable to most sites, with the exceptions noted for the D23N fibrils and Zn^{2+}-induced aggregates at the G9 position. Relatively significant variations exist in the parameters of the motions such as the conformational exchange rate constants and diffusion coefficients of the slower diffusion free states. All the protein sequences also display sigmoidal behavior in the fraction of the bound state upon lowering the temperature as well as variability in the midpoints of the freezing curves.

The patterns of mobility modulations in all the variants are complex; however, certain essential features emerge from the analysis, as summarized in Table 1. The pS8 fibrils, which were determined to have accelerated seeded fibrillation kinetics and enhanced toxicities as well as a more rigid core and a more structured N-terminus than the wild-type protein using structural techniques (33), appear to have the most rigid dynamics. Because of a larger extent of intrastrand contacts in the structure between the N-terminal domain and the core for the fibrils in pS8, one might also expect a larger value of σ for the G9 site, but this is not the case based on the experimental data. The ΔE3 fibrils tend toward higher mobility at the G9 site in line with the morphological fragmentation. A morphologically similar fragmentation is observed for the fibrils in the presence of the cyclization to the pyroglutamate-3 (49) (see also Fig. S4), suggesting that similar changes in the N-terminal dynamics are likely to be present for this PTM as well. There is no clear pattern for the isoD7 fibrils cross-seeded with wild-type Aβ, which has a mixture of changed dynamical features. The most drastic change is seen for the value of T_m at the G9 site, which is ~15–20° lower than for most of the other types of fibrils. This underscores the need for high resolution structural data for the isoD7 fibrils. Based on the structural, kinetics, morphological, and N-terminal dynamics information available for the ΔE3, pyroglutamate-3, pS8, and isoD7 variants (11,32,33,42,49,50,91), all these PTMs are likely to have different cross-seeding abilities, which remains to be elucidated in follow-up work.

For the β-bend region mutation, the most interesting observation is that the modulation of the dynamics compared with the wild-type protein appears to occur closer to the N-terminal end. Indeed, many of the changes toward the restriction of the dynamics can be seen at the F4 site rather than the G9 site. The salt bridge involving E3 may play a role in this restriction for the case of E22Δ. However, no such salt bridge was seen for the antiparallel β-sheet structure of the D23N fibrils. In general, these mutations lead to a less compact fibrils core (30), and thus, the restriction of the dynamics cannot be explained solely by the structural features in this case. Moreover, the p_{bound} value at the F4 site of the D23N fibrils is considerably lower than those of the other residues (Fig. 6). However, this does not indicate an enhancement of the dynamics compared with the other fibrils as the line shapes are significantly wider because of the slow exchange dynamics. The Zn^{2+}-induced aggregates have a clear pattern of overall enhanced mobility in the N-terminus with more pronounced changes at the G9 sites, which is in line with the expectation

TABLE 1 Summary of the Most Essential Changes (with at Least Three SDs) Compared with the Wild-Type

Variant	Parameters Significantly Different from the Wild-Type Fibrils	Overall Conclusion
pS8	$k_{ex,1}$-G9, D_2-G9, T_m-G9	Most rigid of all fibrils at G9, in line with structural information
ΔE3	T_m-G9, $k_{ex,2}$-G9	Tendency toward higher mobility at G9, in line with morphology fragmentation
isoD7 cross-seeded with wild-type	p_{bound}-F4, $k_{ex,1}$-G9, T_m-G9	Mixture of higher and lower mobility features; no clear patterns
D23N	T_m-F4; $k_{ex,1}$-F4, σ-F4, $k_{ex,2}$-F4, T_m-G9, no fast diffusion state for G9, $k_{ex,2}$-G9	Most differences of all fibrils at F4 (more rigid)
E22Δ	D_2-F4, $k_{ex,2}$-F4, $k_{ex,1}$-F4, $k_{ex,1}$-G9	Significant differences at F4 toward rigidity
Zn^{2+} aggregates	$k_{ex,1}$ − F4, no bound state exchange for G9, T_m-G9, p_{bound}-G9, D_2-G9	Overall enhanced mobility but more so at G9 site

The change toward the more rigid value is underlined with the solid lines; the change toward more enhanced dynamics is underlined with the dashed lines.

that the hydrophobic core is less defined in these types of amorphous aggregates, leading to weaker interactions with the N-terminal domain.

Overall, these changes indicate that the dynamics information is complementary to the structural data, and often, it is not straightforward to predict in which direction the dynamics will change upon structural modifications. The results imply that the presence of intricate conformational ensembles can play an important role in the onset of aggregation-prone states and in the differentiation of cross-seeding aggressiveness, thus contributing to the overall polymorphism paradigm. Similar conformational exchange processes may be present in the toxic oligomeric forms as conformational exchange has been detected for the monomer on the surface of the protofibrils by solution NMR measurements (73,74). Our study underlines the need to consider both structural and dynamics information when characterizing the disordered regions of the various toxic variants of Aβ and other aggregation-prone proteins along AD pathways.

SUPPORTING MATERIAL

Supporting Material can be found online at https://doi.org/10.1016/j.bpj.2019.09.004.

AUTHOR CONTRIBUTIONS

L.V. conceived and coordinated the project, designed and performed NMR experiments, and wrote the article with input from all the authors. D.F.A. prepared some of the fibrils samples and performed TEM analysis with contribution from B.K. and performed some of the NMR measurements. Z.-w.H. prepared pS8 fibrils. W.Q. prepared D23N fibrils and performed MPL TEM measurements and analysis. D.O. performed modeling with input from L.V. R.F. contributed to the development of NMR methodology and data collection. All authors discussed the results.

ACKNOWLEDGMENTS

This work was supported by a National Institutes of Health grant 1R15-GM111681 and National Science Foundation grant 1726947. Some of the experiments were performed at the National High Magnetic Field Laboratory, which is supported by National Science Foundation Cooperative Agreement NSF/DMR-1644779, the State of Florida, and the United States Department of Energy.

SUPPORTING CITATIONS

References (92–101) appear in the Supporting Material.

REFERENCES

1. Hardy, J., and D. J. Selkoe. 2002. The amyloid hypothesis of Alzheimer's disease: progress and problems on the road to therapeutics. *Science.* 297:353–356.
2. Barykin, E. P., V. A. Mitkevich, …, A. A. Makarov. 2017. Amyloid β modification: a key to the sporadic Alzheimer's disease? *Front. Genet.* 8:58.
3. Musiek, E. S., and D. M. Holtzman. 2015. Three dimensions of the amyloid hypothesis: time, space and 'wingmen'. *Nat. Neurosci.* 18:800–806.
4. Hardy, J. A., and G. A. Higgins. 1992. Alzheimer's disease: the amyloid cascade hypothesis. *Science.* 256:184–185.
5. Paravastu, A. K., R. D. Leapman, …, R. Tycko. 2008. Molecular structural basis for polymorphism in Alzheimer's beta-amyloid fibrils. *Proc. Natl. Acad. Sci. USA.* 105:18349–18354.
6. Tycko, R. 2015. Amyloid polymorphism: structural basis and neurobiological relevance. *Neuron.* 86:632–645.
7. Qiang, W., W. M. Yau, …, R. Tycko. 2017. Structural variation in amyloid-β fibrils from Alzheimer's disease clinical subtypes. *Nature.* 541:217–221.
8. Lu, J. X., W. Qiang, …, R. Tycko. 2013. Molecular structure of β-amyloid fibrils in Alzheimer's disease brain tissue. *Cell.* 154:1257–1268.
9. Rasmussen, J., J. Mahler, …, M. Jucker. 2017. Amyloid polymorphisms constitute distinct clouds of conformational variants in different etiological subtypes of Alzheimer's disease. *Proc. Natl. Acad. Sci. USA.* 114:13018–13023.
10. Hubin, E., N. A. J. van Nuland, …, K. Pauwels. 2014. Transient dynamics of Aβ contribute to toxicity in Alzheimer's disease. *Cell. Mol. Life Sci.* 71:3507–3521.
11. Roher, A. E., T. A. Kokjohn, …, T. G. Beach. 2017. APP/Aβ structural diversity and Alzheimer's disease pathogenesis. *Neurochem. Int.* 110:1–13.
12. Kummer, M. P., and M. T. Heneka. 2014. Truncated and modified amyloid-beta species. *Alzheim. Res. Ther.* 6:28.
13. Gessel, M. M., S. Bernstein, …, M. T. Bowers. 2012. Familial Alzheimer's disease mutations differentially alter amyloid β-protein oligomerization. *ACS Chem. Neurosci.* 3:909–918.
14. Hatami, A., S. Monjazeb, …, C. G. Glabe. 2017. Familial Alzheimer's disease mutations within the amyloid precursor protein alter the aggregation and conformation of the amyloid-β peptide. *J. Biol. Chem.* 292:3172–3185.
15. Jang, H., F. T. Arce, …, R. Nussinov. 2013. Familial Alzheimer's disease Osaka mutant (ΔE22) β-barrels suggest an explanation for the different Aβ1-40/42 preferred conformational states observed by experiment. *J. Phys. Chem. B.* 117:11518–11529.
16. Baumketner, A., S. L. Bernstein, …, J. E. Shea. 2006. Structure of the 21-30 fragment of amyloid beta-protein. *Protein Sci.* 15:1239–1247.
17. Bush, A. I. 2013. The metal theory of Alzheimer's disease. *J. Alzheimers Dis.* 33 (*Suppl 1*):S277–S281.
18. Hamley, I. W. 2012. The amyloid beta peptide: a chemist's perspective. Role in Alzheimer's and fibrillization. *Chem. Rev.* 112:5147–5192.
19. Ayton, S., P. Lei, and A. I. Bush. 2015. Biometals and their therapeutic implications in Alzheimer's disease. *Neurotherapeutics.* 12:109–120.
20. Suh, S. W., K. B. Jensen, …, C. J. Frederickson. 2000. Histochemically-reactive zinc in amyloid plaques, angiopathy, and degenerating neurons of Alzheimer's diseased brains. *Brain Res.* 852:274–278.
21. Lovell, M. A., J. D. Robertson, …, W. R. Markesbery. 1998. Copper, iron and zinc in Alzheimer's disease senile plaques. *J. Neurol. Sci.* 158:47–52.
22. Paravastu, A. K., I. Qahwash, …, R. Tycko. 2009. Seeded growth of beta-amyloid fibrils from Alzheimer's brain-derived fibrils produces a distinct fibril structure. *Proc. Natl. Acad. Sci. USA.* 106:7443–7448.
23. Ovchinnikova, O. Y., V. H. Finder, …, R. Glockshuber. 2011. The Osaka FAD mutation E22Δ leads to the formation of a previously unknown type of amyloid β fibrils and modulates Aβ neurotoxicity. *J. Mol. Biol.* 408:780–791.
24. Schütz, A. K., T. Vagt, …, B. H. Meier. 2015. Atomic-resolution three-dimensional structure of amyloid β fibrils bearing the Osaka mutation. *Angew. Chem. Int. Ed. Engl.* 54:331–335.
25. Cloe, A. L., J. P. Orgel, …, S. C. Meredith. 2011. The Japanese mutant Aβ (ΔE22-Aβ(1-39)) forms fibrils instantaneously, with low-thioflavin

T fluorescence: seeding of wild-type Aβ(1-40) into atypical fibrils by ΔE22-Aβ(1-39). *Biochemistry.* 50:2026–2039.

26. Tomiyama, T., T. Nagata, …, H. Mori. 2008. A new amyloid beta variant favoring oligomerization in Alzheimer's-type dementia. *Ann. Neurol.* 63:377–387.
27. Grabowski, T. J., H. S. Cho, …, S. M. Greenberg. 2001. Novel amyloid precursor protein mutation in an Iowa family with dementia and severe cerebral amyloid angiopathy. *Ann. Neurol.* 49:697–705.
28. Qiang, W., W. M. Yau, and R. Tycko. 2011. Structural evolution of Iowa mutant β-amyloid fibrils from polymorphic to homogeneous states under repeated seeded growth. *J. Am. Chem. Soc.* 133:4018–4029.
29. Tycko, R., K. L. Sciarretta, …, S. C. Meredith. 2009. Evidence for novel beta-sheet structures in Iowa mutant beta-amyloid fibrils. *Biochemistry.* 48:6072–6084.
30. Qiang, W., W. M. Yau, …, R. Tycko. 2012. Antiparallel β-sheet architecture in Iowa-mutant β-amyloid fibrils. *Proc. Natl. Acad. Sci. USA.* 109:4443–4448.
31. Sgourakis, N. G., W. M. Yau, and W. Qiang. 2015. Modeling an in-register, parallel "Iowa" aβ fibril structure using solid-state NMR data from labeled samples with rosetta. *Structure.* 23:216–227.
32. Hu, Z. W., M. R. Ma, …, Y. M. Li. 2017. Phosphorylation at Ser^{8} as an intrinsic regulatory switch to regulate the morphologies and structures of Alzheimer's 40-residue β-Amyloid (Aβ40) fibrils. *J. Biol. Chem.* 292:2611–2623.
33. Hu, Z. W., L. Vugmeyster, …, W. Qiang. 2019. Molecular structure of an N-terminal phosphorylated β-amyloid fibril. *Proc. Natl. Acad. Sci. USA.* 116:11253–11258.
34. Kumar, S., and J. Walter. 2011. Phosphorylation of amyloid beta (Aβ) peptides - a trigger for formation of toxic aggregates in Alzheimer's disease. *Aging (Albany N.Y.).* 3:803–812.
35. Kumar, S., O. Wirths, …, J. Walter. 2013. Early intraneuronal accumulation and increased aggregation of phosphorylated Abeta in a mouse model of Alzheimer's disease. *Acta Neuropathol.* 125:699–709.
36. Rijal Upadhaya, A., I. Kosterin, …, D. R. Thal. 2014. Biochemical stages of amyloid-β peptide aggregation and accumulation in the human brain and their association with symptomatic and pathologically preclinical Alzheimer's disease. *Brain.* 137:887–903.
37. Kumar, S., N. Rezaei-Ghaleh, …, J. Walter. 2011. Extracellular phosphorylation of the amyloid β-peptide promotes formation of toxic aggregates during the pathogenesis of Alzheimer's disease. *EMBO J.* 30:2255–2265.
38. Tsvetkov, P. O., I. A. Popov, …, S. A. Kozin. 2008. Isomerization of the Asp7 residue results in zinc-induced oligomerization of Alzheimer's disease amyloid beta(1-16) peptide. *ChemBioChem.* 9:1564–1567.
39. Kozin, S. A., I. B. Cheglakov, …, A. A. Makarov. 2013. Peripherally applied synthetic peptide isoAsp7-Aβ(1-42) triggers cerebral β-amyloidosis. *Neurotox. Res.* 24:370–376.
40. Roher, A. E., J. D. Lowenson, …, M. J. Ball. 1993. Structural alterations in the peptide backbone of beta-amyloid core protein may account for its deposition and stability in Alzheimer's disease. *J. Biol. Chem.* 268:3072–3083.
41. Kuo, Y. M., S. Webster, …, A. E. Roher. 1998. Irreversible dimerization/tetramerization and post-translational modifications inhibit proteolytic degradation of A beta peptides of Alzheimer's disease. *Biochim. Biophys. Acta.* 1406:291–298.
42. Fukuda, H., T. Shimizu, …, T. Shirasawa. 1999. Synthesis, aggregation, and neurotoxicity of the Alzheimer's Abeta1-42 amyloid peptide and its isoaspartyl isomers. *Bioorg. Med. Chem. Lett.* 9:953–956.
43. Fabian, H., G. I. Szendrei, …, L. Otvös, Jr. 1994. Synthetic post-translationally modified human A beta peptide exhibits a markedly increased tendency to form beta-pleated sheets in vitro. *Eur. J. Biochem.* 221:959–964.
44. Fonseca, M. I., E. Head, …, A. J. Tenner. 1999. The presence of isoaspartic acid in beta-amyloid plaques indicates plaque age. *Exp. Neurol.* 157:277–288.
45. Chen, B., K. R. Thurber, …, R. Tycko. 2009. Measurement of amyloid fibril mass-per-length by tilted-beam transmission electron microscopy. *Proc. Natl. Acad. Sci. USA.* 106:14339–14344.
46. Pike, C. J., M. J. Overman, and C. W. Cotman. 1995. Amino-terminal deletions enhance aggregation of beta-amyloid peptides in vitro. *J. Biol. Chem.* 270:23895–23898.
47. Dunys, J., A. Valverde, and F. Checler. 2018. Are N- and C-terminally truncated Aβ species key pathological triggers in Alzheimer's disease? *J. Biol. Chem.* 293:15419–15428.
48. Güntert, A., H. Döbeli, and B. Bohrmann. 2006. High sensitivity analysis of amyloid-beta peptide composition in amyloid deposits from human and PS2APP mouse brain. *Neuroscience.* 143:461–475.
49. Wulff, M., M. Baumann, …, M. Fändrich. 2016. Enhanced fibril fragmentation of N-terminally truncated and pyroglutamyl-modified Aβ peptides. *Angew. Chem. Int. Ed. Engl.* 55:5081–5084.
50. Scheidt, H. A., J. Adler, …, D. Huster. 2016. Fibrils of truncated pyroglutamyl-modified Aβ peptide exhibit a similar structure as wild-type mature Aβ fibrils. *Sci. Rep.* 6:33531.
51. Mazzitelli, S., F. Filipello, …, M. Matteoli. 2016. Amyloid-β 1-24 C-terminal truncated fragment promotes amyloid-β 1-42 aggregate formation in the healthy brain. *Acta Neuropathol. Commun.* 4:110.
52. Brännström, K., A. Öhman, …, A. Olofsson. 2014. The N-terminal region of amyloid β controls the aggregation rate and fibril stability at low pH through a gain of function mechanism. *J. Am. Chem. Soc.* 136:10956–10964.
53. Morris, C., S. Cupples, …, D. Du. 2018. N-terminal charged residues of Amyloid-β peptide modulate amyloidogenesis and interaction with lipid membrane. *Chemistry.* 24:9494–9498.
54. Nussbaum, J. M., S. Schilling, …, G. S. Bloom. 2012. Prion-like behaviour and tau-dependent cytotoxicity of pyroglutamylated amyloid-β. *Nature.* 485:651–655.
55. Kummer, M. P., M. Hermes, …, M. T. Heneka. 2011. Nitration of tyrosine 10 critically enhances amyloid β aggregation and plaque formation. *Neuron.* 71:833–844.
56. Rezaei-Ghaleh, N., M. Amininasab, …, M. Zweckstetter. 2016. Phosphorylation modifies the molecular stability of β-amyloid deposits. *Nat. Commun.* 7:11359.
57. Xu, L., R. Nussinov, and B. Ma. 2016. Allosteric stabilization of the amyloid-β peptide hairpin by the fluctuating N-terminal. *Chem. Commun. (Camb.).* 52:1733–1736.
58. Scheidt, H. A., I. Morgado, …, D. Huster. 2012. Dynamics of amyloid β fibrils revealed by solid-state NMR. *J. Biol. Chem.* 287:2017–2021.
59. Lührs, T., C. Ritter, …, R. Riek. 2005. 3D structure of Alzheimer's amyloid-beta(1-42) fibrils. *Proc. Natl. Acad. Sci. USA.* 102:17342–17347.
60. Petkova, A. T., W. M. Yau, and R. Tycko. 2006. Experimental constraints on quaternary structure in Alzheimer's beta-amyloid fibrils. *Biochemistry.* 45:498–512.
61. Bertini, I., L. Gonnelli, …, A. Nesi. 2011. A new structural model of Aβ40 fibrils. *J. Am. Chem. Soc.* 133:16013–16022.
62. Olofsson, A., A. E. Sauer-Eriksson, and A. Ohman. 2006. The solvent protection of alzheimer amyloid-beta-(1-42) fibrils as determined by solution NMR spectroscopy. *J. Biol. Chem.* 281:477–483.
63. Whittemore, N. A., R. Mishra, …, E. H. Serpersu. 2005. Hydrogen-deuterium (H/D) exchange mapping of Abeta 1-40 amyloid fibril secondary structure using nuclear magnetic resonance spectroscopy. *Biochemistry.* 44:4434–4441.
64. Prade, E., C. Barucker, …, B. Reif. 2016. Sulindac sulfide induces the formation of large oligomeric aggregates of the Alzheimer's disease Amyloid-β peptide which exhibit reduced neurotoxicity. *Biochemistry.* 55:1839–1849.

65. Linser, R., R. Sarkar, …, B. Reif. 2014. Dynamics in the solid-state: perspectives for the investigation of amyloid aggregates, membrane proteins and soluble protein complexes. *J. Biomol. NMR.* 59:1–14.

66. Wang, T., H. Jo, …, M. Hong. 2017. Water distribution, dynamics, and interactions with Alzheimer's β-amyloid fibrils investigated by solid-state NMR. *J. Am. Chem. Soc.* 139:6242–6252.

67. Török, M., S. Milton, …, R. Langen. 2002. Structural and dynamic features of Alzheimer's Abeta peptide in amyloid fibrils studied by site-directed spin labeling. *J. Biol. Chem.* 277:40810–40815.

68. Kheterpal, I., S. Zhou, …, R. Wetzel. 2000. Abeta amyloid fibrils possess a core structure highly resistant to hydrogen exchange. *Proc. Natl. Acad. Sci. USA.* 97:13597–13601.

69. Wang, S. S., S. A. Tobler, …, E. J. Fernandez. 2003. Hydrogen exchange-mass spectrometry analysis of beta-amyloid peptide structure. *Biochemistry.* 42:9507–9514.

70. Kheterpal, I., M. Chen, …, R. Wetzel. 2006. Structural differences in Abeta amyloid protofibrils and fibrils mapped by hydrogen exchange–mass spectrometry with on-line proteolytic fragmentation. *J. Mol. Biol.* 361:785–795.

71. Sawaya, M. R., S. Sambashivan, …, D. Eisenberg. 2007. Atomic structures of amyloid cross-beta spines reveal varied steric zippers. *Nature.* 447:453–457.

72. Liu, H., C. Morris, …, D. Du. 2018. Residue-specific dynamics and local environmental changes in Aβ40 oligomer and fibril formation. *Angew. Chem. Int. Ed. Engl.* 57:8017–8021.

73. Fawzi, N. L., D. S. Libich, …, G. M. Clore. 2014. Characterizing methyl-bearing side chain contacts and dynamics mediating amyloid β protofibril interactions using ^{13}C(methyl)-DEST and lifetime line broadening. *Angew. Chem. Int. Ed. Engl.* 53:10345–10349.

74. Fawzi, N. L., J. Ying, …, G. M. Clore. 2011. Atomic-resolution dynamics on the surface of amyloid-β protofibrils probed by solution NMR. *Nature.* 480:268–272.

75. Vugmeyster, L., D. F. Au, …, R. Fu. 2019. Deuteron solid-state NMR relaxation measurements reveal two distinct conformational exchange processes in the disordered N-terminal domain of amyloid-β fibrils. *Chemphyschem.* 20:1680–1689.

76. Au, D. F., D. Ostrovsky, …, L. Vugmeyster. 2019. Solid-state NMR reveals a comprehensive view of the dynamics of the flexible, disordered N-terminal domain of amyloid-β fibrils. *J. Biol. Chem.* 294:5840–5853.

77. Xiao, Y., B. Ma, …, Y. Ishii. 2015. Aβ(1-42) fibril structure illuminates self-recognition and replication of amyloid in Alzheimer's disease. *Nat. Struct. Mol. Biol.* 22:499–505.

78. Vold, R. L., and R. R. Vold. 1991. Deuterium relaxation in molecular solids. *In* Advances in Magnetic and Optical Resonance. W. Warren, ed. Academic Press, pp. 85–171.

79. Vugmeyster, L., and D. Ostrovsky. 2019. Deuterium rotating frame NMR relaxation measurements in the solid state under static conditions for quantification of dynamics. *Chemphyschem.* 20:333–342.

80. Larsen, F. H., H. J. Jakobsen, …, N. C. Nielsen. 1998. High-field QCPMG-MAS NMR of half-integer quadrupolar nuclei with large quadrupole couplings. *Mol. Phys.* 95:1185–1195.

81. Petkova, A. T., R. D. Leapman, …, R. Tycko. 2005. Self-propagating, molecular-level polymorphism in Alzheimer's beta-amyloid fibrils. *Science.* 307:262–265.

82. Noy, D., I. Solomonov, …, I. Sagi. 2008. Zinc-amyloid beta interactions on a millisecond time-scale stabilize non-fibrillar Alzheimer-related species. *J. Am. Chem. Soc.* 130:1376–1383.

83. Vugmeyster, L., M. A. Clark, …, G. L. Hoatson. 2016. Flexibility and solvation of amyloid-β hydrophobic core. *J. Biol. Chem.* 291:18484–18495.

84. Iadanza, M. G., M. P. Jackson, …, N. A. Ranson. 2016. MpUL-multi: software for calculation of amyloid fibril mass per unit length from TB-TEM images. *Sci. Rep.* 6:21078.

85. Kurouski, D. 2016. Supramolecular organization of amyloid fibrils. *In* Exploring New Findings on Amyloidosis. A.-M. Fernandez-Escamilla, ed. InTech.

86. Palmer, A. G., III 2014. Chemical exchange in biomacromolecules: past, present, and future. *J. Magn. Reson.* 241:3–17.

87. Schanda, P., and M. Ernst. 2016. Studying dynamics by magic-angle spinning solid-state NMR spectroscopy: principles and applications to biomolecules. *Prog. Nucl. Magn. Reson. Spectrosc.* 96:1–46.

88. Tollinger, M., A. C. Sivertsen, …, P. Schanda. 2012. Site-resolved measurement of microsecond-to-millisecond conformational-exchange processes in proteins by solid-state NMR spectroscopy. *J. Am. Chem. Soc.* 134:14800–14807.

89. Krushelnitsky, A., D. Gauto, …, K. Saalwächter. 2018. Microsecond motions probed by near-rotary-resonance $R_{1\rho}$ ^{15}N MAS NMR experiments: the model case of protein overall-rocking in crystals. *J. Biomol. NMR.* 71:53–67.

90. Li, K., P. S. Emani, …, G. P. Drobny. 2014. A study of phenylalanine side-chain dynamics in surface-adsorbed peptides using solid-state deuterium NMR and rotamer library statistics. *J. Am. Chem. Soc.* 136:11402–11411.

91. Adler, J., H. A. Scheidt, …, D. Huster. 2014. Local interactions influence the fibrillation kinetics, structure and dynamics of Aβ(1-40) but leave the general fibril structure unchanged. *Phys. Chem. Chem. Phys.* 16:7461–7471.

92. Harris, J. R., and J. W. Horne. 1991. Negative staining. *In* Electron Microscopy in Biology. J. R. Harris, ed. IRL Press, pp. 203–228.

93. Dubochet, J., M. Groom, and S. Mueller-Neuteboom. 1982. The mounting of macromolecules for electron microscopy with particular reference to surface phenomena and the treatment of support films by glow discharge. *In* Advances in Optical and Electron Microscopy. R. Barrer and V. E. Cosslett, eds. Academic Press, pp. 107–135.

94. Gor'kov, P. L., E. Y. Chekmenev, …, W. W. Brey. 2007. Using low-E resonators to reduce RF heating in biological samples for static solid-state NMR up to 900 MHz. *J. Magn. Reson.* 185:77–93.

95. Persson, P.-O., and G. Strang. 2004. A simple mesh generator in MATLAB. *SIAM Rev.* 46:329–345.

96. Namba, K., and G. Stubbs. 1986. Structure of tobacco mosaic virus at 3.6 A resolution: implications for assembly. *Science.* 231:1401–1406.

97. Parr, W. C., and W. R. Schucany. 1980. Minimum distance and robust estimation. *J. Am. Stat. Assoc.* 75:616–624.

98. Vold, R. L., and G. L. Hoatson. 2009. Effects of jump dynamics on solid state nuclear magnetic resonance line shapes and spin relaxation times. *J. Magn. Reson.* 198:57–72.

99. Vega, A. J. 1992. MAS NMR spin locking of half-integer quadrupolar nuclei. *J. Magn. Reson.* 96:50–68.

100. van der Maarel, J. R. C. 1993. The relaxation dynamics of spin 1=1 nuclei with a static quadrupolar coupling and a radio-frequency field. *J. Chem. Phys.* 99:5646–5653.

101. Abragam, A. 1961. Principles of Nuclear Magnetism. Clarendon Press, Oxford, UK.

Biophysical Journal, Volume *117*

Supplemental Information

Effect of Post-Translational Modifications and Mutations on Amyloid-β Fibrils Dynamics at N Terminus

Liliya Vugmeyster, Dan F. Au, Dmitry Ostrovsky, Brian Kierl, Riqiang Fu, Zhi-wen Hu, and Wei Qiang

Supplementary Material **Effect of Post-translational Modifications and Mutations on Amyloid-β fibrils Dynamics at N-terminus**

Liliya Vugmeyster,[1,]* Dan F. Au,[1] Dmitry Ostrovsky,[2] Brian Kierl,[1] Riqiang Fu,[3] Zhi-wen Hu, [4] Wei Qiang[4]

[1] Department of Chemistry, University of Colorado Denver, Denver CO USA 80204

[2] Department of Mathematics, University of Colorado Denver, Denver CO USA 80204

[3] National High Field Magnetic Laboratory, Tallahassee, FL USA 32310

[4]Department of Chemistry, Binghamton University, Binghamton, New York USA 13902

*To whom correspondence should be addressed: Liliya Vugmeyster, 1201 Laurimer Street, Denver CO 80204, USA email: LILIYA.VUGMEYSTER@UCDENVER.EDU

Supporting file S1. Details of Experimental and Modeling Procedures

I. Peptide synthesis

The $A\beta_{1-40}$ peptides were prepared by using solid-state peptide synthesis (performed by Thermofisher Scientific Co, Rockford, IL). Fluorenylmethyloxycarbonyl (FMOC)-Phenylalanine-ring-d_5 and FMOC-Glycine-C_α-d_2, were purchased from Cambridge Isotopes Laboratories (Andover, MA). The native sequence is DAEFRHDSGYEVHHQKLVFFAEDVGSNKGAIIGLMVGGVV. The following modifications were introduced for the variants: truncation of the first two residues (ΔE3), D7-isoD7 (isoD7), phosphorylation of serine-8 (pS8), E22 deletion mutant (E22Δ), D23 to N substitution (D23N). The peptides were purified by reversed-phase HPLC and their identity and purity were confirmed by mass spectrometry and reversed-phase HPLC.

II. Preparation of fibril samples

The pS8 and ΔE3: fibrils were grown following the generation seeding protocols: To produce parent fibrils (G0), lyophilized peptides were dissolved in hexafluoroisoproponal (HFIP) to 2.0 mg/mL and incubated overnight at ambient temperature. The HFIP was removed by N_2 flow and followed high-vacuum for at least 3 hours. The resultingpeptide film was dissolved in dimethyl sulfoxide (DMSO) to 2.0 mM, sonicated on ice-bath for 3 minutes, centrifuged at 14,000 rpm for 10 minutes to remove any preformed aggregates, and diluted with 10 mM monosodium phosphate buffer (pH 7.4, 0.05% NaN_3) to the final concentration of 0.5 mg/mL. The solution was incubated at 37 ºC with 200 rpm orbital agitation for 72 hours. To obtain the first-generation seeded fibrils (G1), G0 fibrils were sonicated on ice-bath with a probe sonicator for 30-60 seconds (continuous power output, 20% duty cycle). G1 generation was prepared by dissolving the lyophilized peptide in DMSO followed by immediate addition to the phosphate buffer containing G0 seeds in 1:10 molar ratio, with a final peptide concentration of 0.5 mg/mL. G1 fibrils growth was achieved by incubation with gentle 40 rpm orbital agitation for 24 hours at room temperature. The following generations were prepared using the same protocol as for G1, and the last-generation fibrils (G6 for pS8 and G5 for ΔE3) were used as seeds for the NMR bulk samples.

IsoD7 cross-seeded with wild-type $A\beta_{1-40}$: the seeds consisted of the wild-type $A\beta_{1-40}$ fibrils in the 3-fold symmetric polymorph in the phosphate buffer at 0.5 mg/mL concentration. Lyophilized isoD7 $A\beta_{1-40}$ peptide was solubilized in DMSO to 5.0 mM. The seeds were sonicated for 1.5 min using a probe sonicator. A 1:10 molar ratio of the wild-type $A\beta_{1-40}$ seeds to the isoD7. $A\beta_{1-40}$ solubilized peptide was combined in the phosphate buffer to yield a total protein concentration of 0.4 mg/mL and immediately filtered through a 0.22 μm filter. The solution was incubated for 3-5 days with gentle 40 rpm orbital agitation at room temperature.

E22Δ: Lyophilized peptides were dissolved at a 5 mM concentration in DMSO and immediately transferred to the phosphate buffer to the final concentration of 0.3 mg/mL. The fibrils were allowed to grow for at least 4 days at room temperature at quiescent conditions. TEM images were taken immediately upon dissolving in the buffer, at 2-3 hours and at 24-30 hours after dissolution.

Collection and hydration of bulk samples for NMR analysis: The bulk fibrils were pelleted by centrifuging at 300,000 *g* for 7-9 hours. The exceptions were Zn^{2+}-induced aggregates and ΔE3 fibrils, for which the fibrils were collected by centrifugal dialysis using Amicon filters with 3 kDa molecular weight cut-off. Collected fibrils were re-suspended in deionized water, rapidly frozen with liquid nitrogen, and lyophilized. A hydrated state with a water content of 200% by weight was achieved by pipetting deuterium-depleted H_2O. The samples were packed in 5 mm NMR tubes (cut to 21 mm length) using Teflon tape to center the sample volume in the coil of the NMR probe.

III. Negatively-stained transmission electron microscopy

Samples were stored at room temperature and diluted to about 0.1 mg/mL with hydro, millipore-filtered water. Samples were negatively stained by using the drop method (*1*) in the following manner. Four microliter aliquots of the sample, millipore-filtered water, and 2% uranyl acetate aqueous stain were applied sequentially to a freshly glow-discharged,(*2*) Formvar carbon-coated 300 mesh copper grid for the following incubation times: 2 min, 10 sec, and 2 min, respectively. Each 4 μl droplet was removed by wicking with filter paper for 5 sec. The filter paper was blotted prior to the addition of the next droplet. After staining, the grid was air-dried under a vacuum for 20 min. Images were collected under low dose conditions of 120,000× using the FEI Tecnai G2 Spirit Biotwin microscope operating at 80 kV.

IV. NMR spectroscopy

Experiments were performed using 9.4 T (University of Colorado at Denver) and 14.1 T (National High Magnetic Field Laboratory) spectrometers equipped with the Bruker neo consoles and static probes with 5 mm diameter coils: the wide-line low-E probe(*3*) for the 14.1 T spectrometer and the Phoenix probe for the 9.6 T spectrometer.

Line shape experiments were performed with a quadrupole echo pulse sequence based on an eight-step phase cycle(*4*), with a delay of 31-36 μs between 90° pulses. A line broadening function of 0.5 to 2 kHz was employed to enhance the signal.

The $R_{1\rho}$ experiments were performed at 9.4 T and 37°C using the methodology described in previous work(*5*) with the pulse sequence of Figure S1. Spin-lock times varied between 200 μs and 15 ms (a total of 12 relaxation delays) and powers ranged between 5 and 20 kHz. The upper limit was determined by the sensitivity of the sample to heating. The number of scans varied between 2048 and 8000 depending on each sample's sensitivity.

^2H QCPMG time-domain measurements (*6*) were performed at 14.1 T field strength and 37°C. The pulse sequence used for the time domain acquisition(*7*) and further experimental details are shown in Figure S1. The multiple echo acquisition scheme employed echo times between 53 and 363 μs with the rf irradiation frequency set exactly on resonance. The lower limit of the pulse spacing was determined by system electronic/acoustical ringing, while the upper limit was determined by sensitivity factors. The number of scans varied between 4096 and 81920 depending on the signal-to-noise ratio in each sample. The inter-scan delay was set to 0.2-0.4 sec and 32 dummy scans were utilized.

V. Motional modeling and fitting of the data

Motional modeling followed the protocols described previously.(*5, 7, 8*) Below we present an overview of the procedures.

Theory overview

Density matrix for the spin-1 system can be written in the basis of the following operators(*9*)

$$\hat{S}_x = \frac{1}{2}\begin{pmatrix} 0 & 1 & 0 \\ 1 & 0 & 1 \\ 0 & 1 & 0 \end{pmatrix}, \hat{S}_y = \frac{1}{2}\begin{pmatrix} 0 & -i & 0 \\ i & 0 & -i \\ 0 & i & 0 \end{pmatrix}, \hat{J}_x = \frac{1}{2}\begin{pmatrix} 0 & -i & 0 \\ i & 0 & i \\ 0 & -i & 0 \end{pmatrix}, \hat{J}_y = \frac{1}{2}\begin{pmatrix} 0 & 1 & 0 \\ 1 & 0 & -1 \\ 0 & -1 & 0 \end{pmatrix} \quad \text{(S-1)}$$

$$\hat{S}_z = \frac{1}{\sqrt{2}}\begin{pmatrix} 1 & 0 & 0 \\ 0 & 0 & 0 \\ 0 & 0 & -1 \end{pmatrix}, \hat{J}_z = \frac{1}{\sqrt{2}}\begin{pmatrix} 0 & 0 & -i \\ 0 & 0 & 0 \\ i & 0 & 0 \end{pmatrix}, \hat{Q} = \frac{1}{\sqrt{6}}\begin{pmatrix} 1 & 0 & 0 \\ 0 & -2 & 0 \\ 0 & 0 & 1 \end{pmatrix}, \hat{K} = \frac{1}{\sqrt{2}}\begin{pmatrix} 0 & 0 & 1 \\ 0 & 0 & 0 \\ 1 & 0 & 0 \end{pmatrix}$$

They obey the following normalization condition $\mathrm{tr}(O_k^{+}O_l) = \delta_{kl}$.

During the saturation period and in the frame rotating with the Larmor frequency the secular part of the Hamiltonian is given by:

$$\hat{H}_{sec} = \sqrt{\frac{2}{3}}\omega_Q \hat{Q} + \sqrt{2}\omega_{RF}\hat{S}_x,$$

where ω_{RF} is the RF field strength.

$$\omega_Q = \frac{3\pi}{2} C_q \left(\frac{3\cos^2\theta - 1}{2} + \frac{\eta}{2}\sin^2\theta\cos 2\phi\right) \quad \text{(S-2)}$$

is the frequency of the secular part of quadrupole interaction with angles (θ, ϕ) representing the rotation of the principal-axis system (PAS) of the quadrupole interaction with respect to the laboratory frame. The quadrupolar coupling constant is given by $C_q = \frac{e^2 qQ}{h}$, and $\eta \equiv \frac{q_{xx} - q_{yy}}{q_{zz}}$ represents the asymmetry of the tensor, defined in the interval $0 \le \eta \le 1$ with $|q_{zz}| \ge |q_{yy}| \ge |q_{xx}|$. eQ is the electric quadrupole moment of the nucleus and eq is the largest component of the electric field gradient.

In the presence of molecular motions, the value of ω_Q for an individual crystallite does not remain constant, but changes due to changes in the PAS orientation. In addition to the dependence of ω_Q originating from molecular motions, in solids powder there is an additional dependence of ω_Q on the orientation of the crystallite to the static magnetic field, as it the case for all anisotropic interactions.
Additional terms in the Hamiltonian include quadrupole interaction terms fluctuating with the single and double Larmor frequencies. They are of less significance in these measurements then relaxation due to fluctuations in the value of ω_Q and are treated separately through the Redfield theory.(*10*)

The evolution of the density matrix can be written using the basis of Eq.(S-1) in the superoperator formalism. Liouville - von Neumann formalism combines the Hamiltonian super-operator for the spin density matrix with Markovian jumps between states with different values of ω_Q simulating various spin environments. It, therefore, includes the relaxation due to the fluctuations in the ω_Q value, which, in general, cannot be treated within the Redfield approximation and the full Liouvillian treatment becomes necessary.(*11*)

If intramolecular motions are given by discrete jumps between *n* sites with different values of ω_Q sampled by the conformational exchange, the evolution matrix becomes

$$\frac{d}{dt}\begin{pmatrix}\rho_1\\ \rho_2\\ \vdots\\ \rho_n\end{pmatrix}=\begin{pmatrix}A_1+K_{11} & K_{12} & \cdots & K_{1n}\\ K_{21} & A_2+K_{22} & \cdots & K_{2n}\\ \vdots & \vdots & \ddots & \vdots\\ K_{n1} & K_{n2} & \cdots & A_n+K_{nn}\end{pmatrix}\begin{pmatrix}\rho_1\\ \rho_2\\ \vdots\\ \rho_n\end{pmatrix} \quad \text{(S-3)}$$

where $\rho_i = (S_x, J_x, K, Q)^T$ are the components of the density matrix for the site *i* in the basis of the operators of Eq.(1) with coefficients corresponding to the components of the density matrix as for the operators themselves, but without hats. The other 4 components of the density matrix are decoupled under both the on-resonance $R_{1\rho}$ and QCPMG conditions used in the experiment.

The 4×4 evolution A_i matrices which include coherent evolution given by $\widehat{H}_{sec}$ are given by:

$$A=\begin{pmatrix}0 & -\omega_q & 0 & 0\\ \omega_q & 0 & -\omega_{sl} & -\sqrt{3}\omega_{sl}\\ 0 & \omega_{sl} & 0 & 0\\ 0 & \sqrt{3}\omega_{sl} & 0 & 0\end{pmatrix} \quad \text{(S-4)}$$

The off-diagonal blocks in Eq.(S-3) represent conformational exchange and are given by $K_{ij} = k_{ij}I$, where *I* is the 4×4 identity matrix and the diagonal blocks $K_{ii} = -\sum_{j\neq i} K_{ji}$ provide conservation of probability.

The exchange matrix K_{ij} combines components responsible for the isotropic diffusion and the conformational exchange between the free diffusion state and the bound state, according to the following scheme:

$$K=\left(\begin{array}{c|c}\text{diffusion} & \begin{array}{c}\text{exchange}\\ \text{with bound}\\ \text{state}\end{array}\\ \hline \text{exchange with bound state} & \end{array}\right)$$

The block of the exchange matrix K_{ij} responsible for the diffusion, is represented by nearest neighbor jumps with sites of equal populations distributed (almost) uniformly on the surface of the sphere and with identical exchange rates between the sites, $K_{ij} = k_D$. We used the program DistMesh,(*12*) which creates the uniform distribution of sites by assuming a linear repulsive force and solving for the equilibrium. The inclusion of $N_D = 192$ sites is sufficient to adequately represent the isotropic diffusion process and this leads to the following range of jump angles in the crystal-fixed frame between the sites: 13.7–18.7°. Due to the spin 1 symmetry properties, only the second-order spatial spherical harmonics give rise to the spectral densities. Thus, the second-order eigenfunction of the Smoluchowski diffusion equation encodes the spatial reorientation and the corresponding eigenvalue is related to the diffusion coefficient *D* as $Dl(l+1) = 6D$. As expected, the simulated eignevalues of K_{ij} appear in groups of $2l+1$, corresponding to the eignevectors with the angular momentum *l* of the continuous limit of the diffusion equation. The five eigenvalues λ_2 corresponding to $l = 2$ are then averaged to obtain the numerical value of *D*. This establishes the correspondence between *D* and k_D as $k_D = 6D/\langle\lambda_2\rangle$.

To include the exchange process, one additional site with a fixed angular position corresponding to the bound state was added to yield a total of $N_D + 1$ sites. The exchange was modeled by jumps between every site describing the spherical diffusion and the bound-state site with an arbitrary fixed angular position with

the rate k_{ex}/N_D. Modeled in this fashion, the relative tensor orientation in the free and bound states is averaged over the uniform spherical distribution.

Computational modeling details

Each of the two exchange process was modeled by jumps between every site describing the spherical diffusion and the bound-state site. The relative weights of each site were expressed through the ratio of the forward and reverse rate constants for the exchange process. Modeling the exchange with two free states and one bound state included two sets of 192 sites describing the surface of two spheres with the corresponding nearest-neighbor jump constants within each set, as well as independent exchange constants between every site of each of the two sets and an arbitrarily fixed site in the crystal-fixed frame, corresponding to the bound state. The direct exchange between the two free states was modeled through pair-wise exchanges between the 192 spherical diffusion sites corresponding to the same orientation in both states. Simulated decays utilized time points identical to those used in the experiment. QCPMG time domain evolution and $R_{1\rho}$ simulations included the full Liouvillian treatment with 200 crystallites. All simulations were performed in Matlab and utilized selected blocks from the EXPRESS program.(*13*) Best fits for the dynamic parameters of the models were determined by minimization of χ^2 for predictions of the model for ^{2}H QCPMG and $R_{1\rho}$ relaxation rates. The errors were obtained by the inverse covariance matrix method calculated with Monte-Carlo sampling of the model parameters. The errors in the sigmoidal curve parameters (Eq. 1 of the main text) for the temperature dependence of p_{bound} were obtained by the inverse covariance matrix method for the mean-squared errors.

VI. Dark-field TEM MPL data collection

Dark-field images can be obtained using a conventional TEM set-up by tilting the incident electron beam by a small angle so that it is blocked by the objective aperture after it encounters the sample. All the dark-field TEM images for the MPL measurements were collected using an FEI Morgagni microscope at 80 kV with unstained samples, using a side-mounted Advanced Microscopy Techniques Advantage HR CCD camera. The TEM samples were prepared using similar protocols as the regular imaging with uranyl acetate staining. The internal standard tobacco mosaic virus (TMV) solution was co-incubated with the fibril solution during the sample deposition to TEM grids. The dark-field TEM images were taken with 44× and 28× magnifications. Images were analyzed with ImageJ software. Only fibrils that appeared to be single filaments were selected for the MPL measurements. For the extraction of the MPL values, image intensities were integrated over rectangular areas of around 80 nm in length centered on the fibril segments. Rectangular widths were chosen to encompass the fibrils. The resulting intensities are denoted by I_{F} below. The background intensities were taken on both sides of each individual fibril segment and denoted by I_{B1} and I_{B2}. The same procedure was employed for the TMV standard, with the individual intensities denoted as I_{TMV} and backgrounds as I_{B3} and I_{B4}. The value of $\langle I_{TMV} \rangle = \langle I_{TMV} - 1/2(I_{B3} + I_{B4} \rangle$ was calculated as an average of all TMV data under the identical tilt angle of the beam. The known value of MPL for TMV (MPL_{TMV}) is 131 kDa/nm (*14*). The MPL values are given by $MPL = \frac{MPL_{TMV}\,(I_F - 1/2(I_{B1} + I_{B2}))}{\langle I_{TMV} \rangle}$. The resulting MPL values were grouped in bins of 2 kDa/nm for the construction of the histograms. The two-Gaussian fit utilized the minimum distance estimation with the Kolmogorov–Smirnov criterion, which confers increased robustness (*15*).

Figures

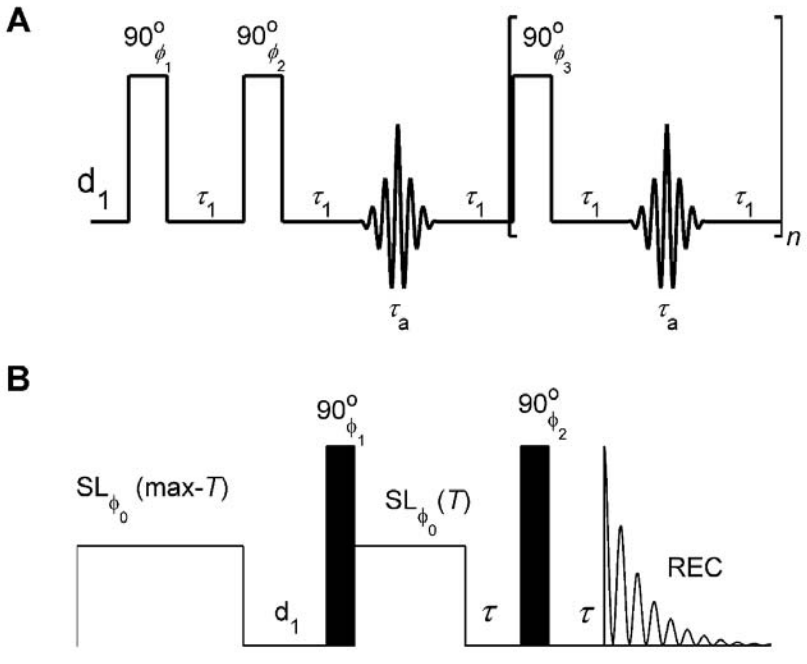

Figure S1. A) The QCPMG pulse sequence for ^{2}H nuclei. Quadrupolar echo block with the 90^o pulses shown as rectangles is followed by a full echo acquisition period (τ_a) and then proceeds to an *n* repeating multiple echo unit (in square brackets). d_1 is the inter-scan delay, and τ_1 is the pulse ringing delay $\tau_{qcpmg} = \tau_a + 2\tau_1 + 90^{\circ}/2$. The analysis of decay curves starts with the first full echo in brackets. The following 16-step phase cycle is used: ϕ_1=*x,y,-x,-y*; ϕ_2= *y,x,y,x,-y,-x,-y,-x*; ϕ_3= *y,x,y,x,-y,-x,-y,-x, -y,-x,-y,-x, y,x,y,x*; ϕ_{rec}= *-x,-y,x,y*. B) Pulse sequence for static ^{2}H solid-state $R_{1\rho}$ measurements. The heat compensation block SL(max-*T*) is followed by the inter-scan delay d_1 and the preparation 90^o pulse, followed by a variable spin-lock delay SL(*T*). The detection is accomplished using the quadrupole echo scheme, $\tau - 90^{o} - \tau$. The phase cycle corresponds to ϕ_0=*x*; ϕ_1= *-y,y*; ϕ_2= *-x,x*; receiver= *-y,y*.

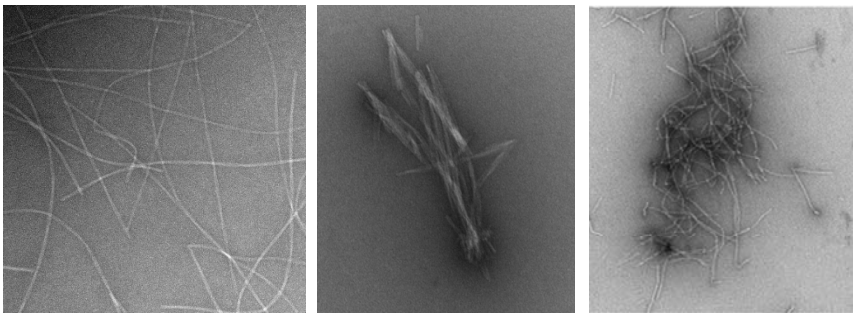

Figure S2. Additional examples of negatively stained TEM images of the mature isoD7 (cross-seeded with the 3-fold wild-type fibrils), ΔE3, and E22Δ $A\beta_{1\text{-}40}$ fibrils.

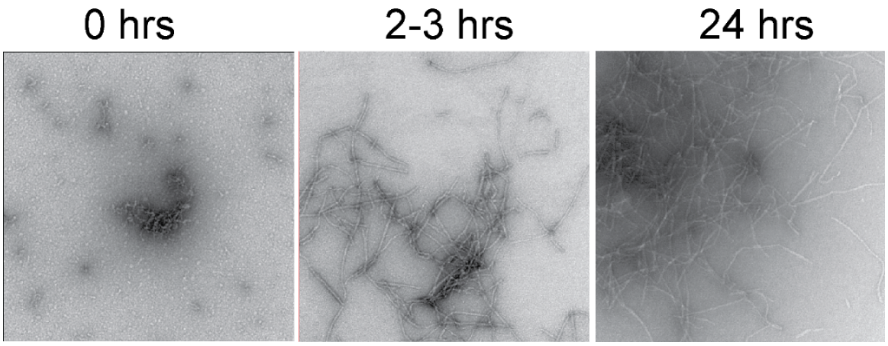

Figure S3. Negatively stained TEM images of the E22Δ $A\beta_{1\text{-}40}$ fibrils at three time point points during the fibril formation process.

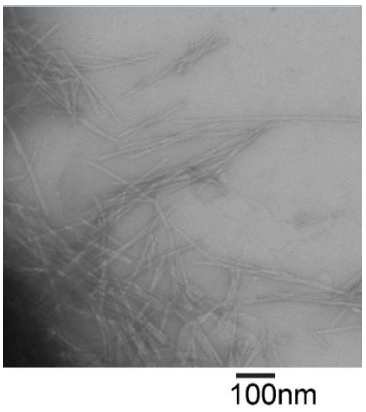

Figure S4. A negatively stained TEM image of the pyroglutamate-3 $A\beta_{1\text{-}40}$ fibrils prepared using the same protocol as the one used for the ΔE3 fibrils.

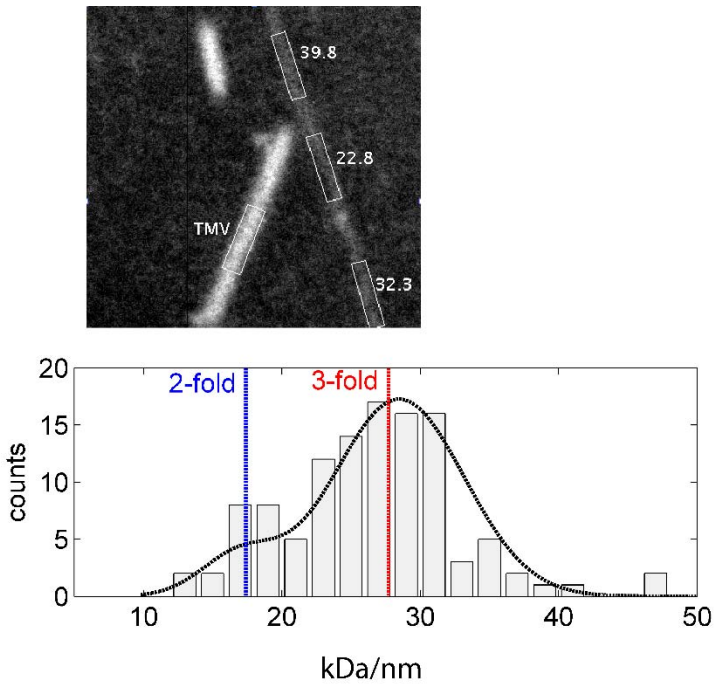

Figure S5. Top panel: Dark-field images of isoD7 amyloid fibrils resulting from the cross-seeding procedure with the wild-type $A\beta_{1\text{-}40}$ in the 3-fold symmetric polymorph. Rectangular areas demonstrate examples of fibril fragments along the long axis chosen for quantitative MPL analysis, with numerical values labeled. Tobacco mosaic virus rods used as standard are labeled "TMV". Bottom panel: Resulting MPL histograms. Vertical dashed lines correspond to the average MPL values of the wild-type 2-fold symmetric polymorph (blue) and 3-fold symmetric polymorph (red), as previously determined by a similar approach (*16*). The fit of MPL data to two Gaussians (dotted black line) are overlaid over the histograms. The fit yielded central values within the ranges for the 3-fold and 2-fold polymorphs with populations of 0.89 and 0.11, with the mean values of 15.9 and 27 kDa/nm, and the widths of half-heights of 6.6 and 11.1 kDa/nm, respectively.

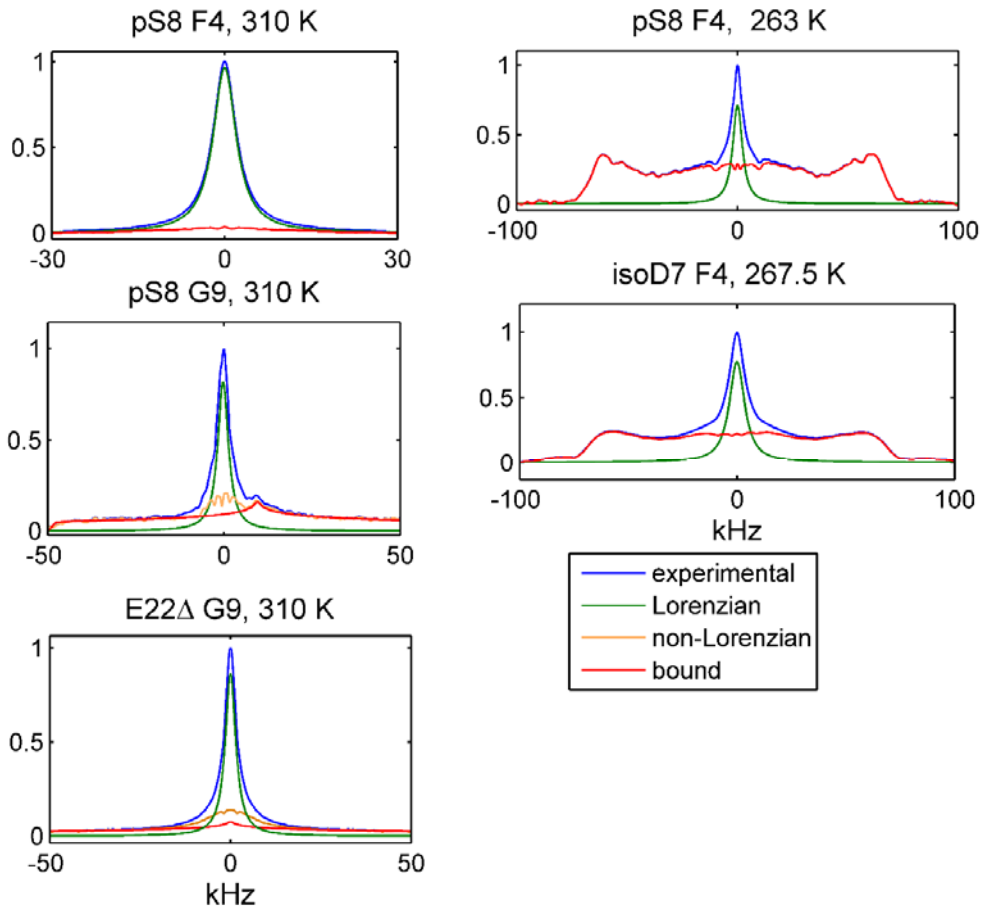

Figure S6. Examples of decomposition of ^{2}H static line shapes into components for determination of the fractions of the bound and free states. For cases in which there is no separate non-Lorentzian line shown, all of the non-Lorenzian component is attributed to the "bound" state.

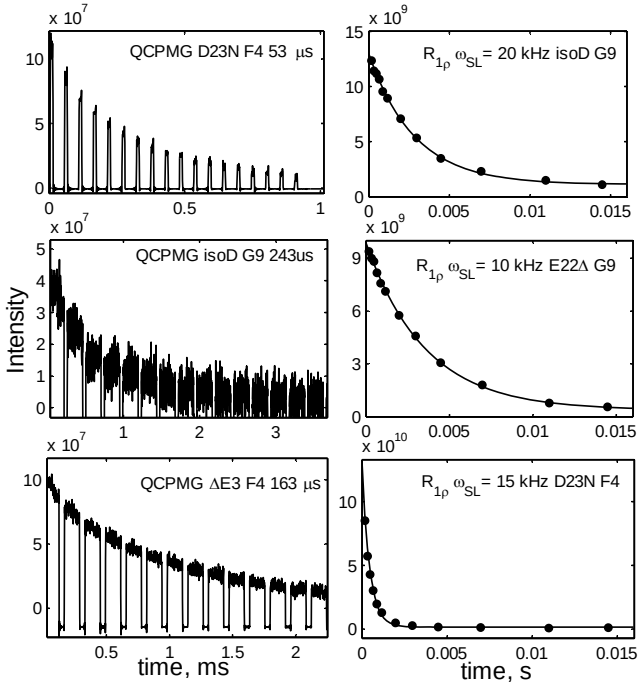

Figure S7. Examples of the experimental magnetization decay curves $M(t)$ obtained from the ^{2}H $R_{1\rho}$ and QCPMG experiments. For the $R_{1\rho}$ experiment, peak intensities are in arbitrary units, obtained via the integration of the central spectral component over the half-height region, versus time (circles). The lines represent the mono-exponential fits of the form $M(t) = Ae^{-t/T_{1\rho}} + B$. For the QCPMG experiment, the examples of the time domain data are shown from the first echo in the loop (designated by the square brackets in the pulse sequence of Figure S5). The type of experiment, variant label, and the values of ω_{SL} or τ_{QCPMG} are shown directly on the graphs.

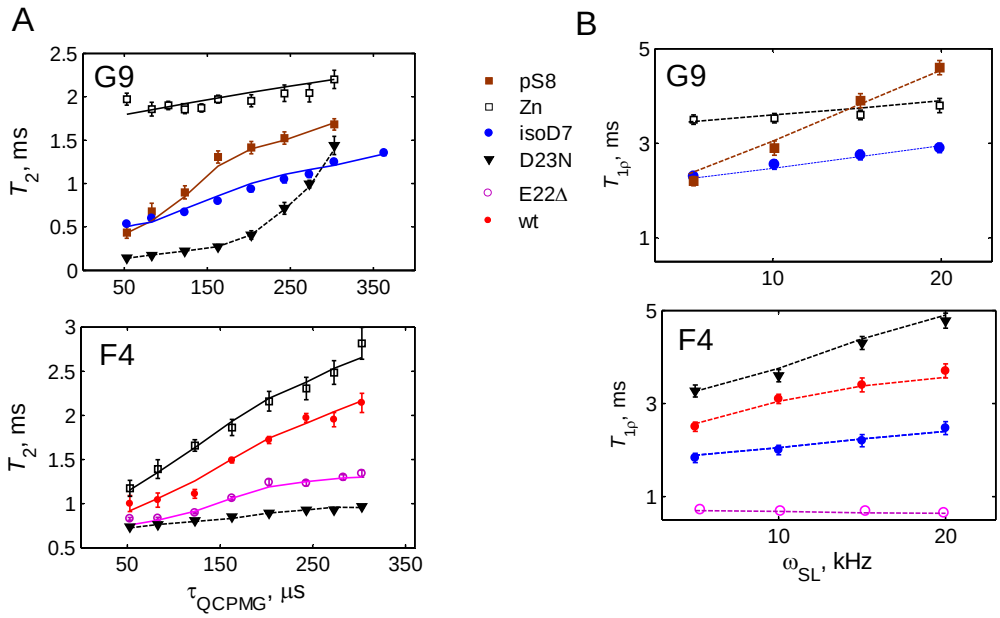

Figure S8. Representative fits of experimental QCPMG rates (A) and ^{2}H $R_{1\rho}$ rates (B). Fits are shown by the lines according to models of Figure 3 of the main text.

References

1. Harris, J. R., and Horne, J. W. (1991) Negative Staining, in Electron Microscopy in Biology (Harris, J. R., Eds.), pp 203-228, Oxford: IRL Press.
2. Dubochet, J., Groom, M., and Mueller-Neuteboom, S. (1082) The mounting of macromolecules for electron microscopy with particular reference to surface phenomena and the treatment of support films by glow discharge., in Adv. Opt. Electron Microsc. (Barrer, R., and Cosslett, V. E., Eds.), pp 107-135.
3. Gor'kov, P. L., Chekmenev, E. Y., Li, C., Cotten, M., Buffy, J. J., Traaseth, N. J., Veglia, G., and Brey, W. W. (2007) Using low-E resonators to reduce RF heating in biological samples for static solid-state NMR up to 900 MHz, J. Magn. Reson. 185, 77-93.
4. Vold, R. L., and Vold, R. R. (1991) Deuterium Relaxation in Molecular Solids, in Advances in Magnetic and Optical Resonance (Warren, W., Ed.), pp 85-171, Acadenic Press, San Diego.
5. Vugmeyster, L., and Ostrovsky, D. (2019) Deuterium Rotating Frame NMR Relaxation Measurements in the Solid State under Static Conditions for Quantification of Dynamics, Chemphyschem. 20, 333-342.
6. Larsen, F. H., Jakobsen, H. J., Ellis, P. D., and Nielsen, N. C. (1998) High-field QCPMG-MAS NMR of half-integer quadrupolar nuclei with large quadrupole couplings, Mol. Phys. 95, 1185-1195.
7. Vugmeyster, L., Au, D. F., Ostrovsky, D., and Fu, R. (2019) Deuteron solid-state NMR relaxation measurements reveal two distinct onformational exchange processes in the disordered N-terminal domain of amyloid-b fibrils, ChemPhysChem. 20, 1680.
8. Au, D. F., Ostrovsky, D., Fu, R., and Vugmeyster, L. (2019) Solid-state NMR reveals a comprehensive view of the dynamics of the flexible, disordered N-terminal domain of amyloid-β fibrils, J. Biol. Chem. 294, 5840–5853.
9. Vega, A. J. (1992) MAS NMR spin locking of half-integer quadrupolar nuclei, J. Magn. Reson. 96, 50-68.
10. van der Maarel, J. R. C. The relaxation dynamics of spin 1=1 nuclei with a static quadrupolar coupling and a radio-frequency field, J Chem Phys 99, 5646-5653.
11. Abragam, A. (1961) Principles of Nuclear Magnetism, Clarendon Press, Oxford.
12. Persson, P.-O., and Strang, G. (2004) A Simple Mesh Generator in MATLAB, SIAM Rev. 46, 329-345.
13. Vold, R. L., and Hoatson, G. L. (2009) Effects of jump dynamics on solid state nuclear magnetic resonance line shapes and spin relaxation times, J. Magn. Reson. 198, 57-72.
14. Namba, K., and Stubbs, G. (1986) Structure of tobacco mosaic virus at 3.6 A resolution: implications for assembly, Science 231, 1401-1406.
15. Parr, W. C., and Schucany, W. R. (1980) Minimum Distance and Robust Estimation, J. Am. Stat. Assoc. 75, 616-624.
16. Chen, B., Thurber, K. R., Shewmaker, F., Wickner, R. B., and Tycko, R. (2009) Measurement of amyloid fibril mass-per-length by tilted-beam transmission electron microscopy, Proc. Natl. Acad. Sci. U.S.A. 106, 14339-14344.